MINISTRY OF AVIATION

AERONAUTICAL RESEARCH COUNCIL
REPORTS AND MEMORANDA

Experiments at $M_0 = 4{\cdot}03$ on Two Families of Pressure-Plotting Wing-and-Half-Cone Combinations

By
E. W. E. Rogers, J. L. Attridge,
Miss A. G. J. Macdonald and J. Callinan

LONDON: HER MAJESTY'S STATIONERY OFFICE

1967

PRICE 18s. 6d. NET

Experiments at $M_0 = 4{\cdot}03$ on Two Families of Pressure-Plotting Wing-and-Half-Cone Combinations

By
E. W. E. Rogers, J. L. Attridge,
Miss A. G. J. Macdonald and J. Callinan

Reports and Memoranda No. 3473*

March, 1964

Summary.

Tests have been made at a Mach number of $4{\cdot}03$ and Reynolds number of $3{\cdot}4$ million on two families of models, consisting of delta wings with underslung half-cone bodies. The wing sweepback angles were 75° and 80°, and the appropriate cone semi-vertex angles tested were 4°, 10° and 13° for the larger wing and 4°, 6·7° and 10° for the smaller wing. The surface distributions were measured at four chordwise stations on all models for incidences between 0° and 9·6° and analysed to provide information on the influence of the wing on the cone flow, and conversely the cone influence on the wing lower- and upper-surface flow.

It was found that near the wing-body junction the resultant pressure was close to that obtained by superposing the wing and body flow fields. On the most windward generator of the cone the wing influence is negligible. For small incidences, the pressure changes due to the cone on the exposed wing under-surface may be predicted by exact cone theory; at all incidences, these pressure changes are linked to the pressures developed on the cone surface near the junction.

The pressure increments were integrated to give the lift and pressure drag acting on the models (base drag excluded) and from these quantities the lift/drag ratio may be found. The highest value of this occurs for the isolated wings, but the ratio is sensitive to model attitude. The combinations which have a large body develop a smaller maximum lift/drag, but the variation of this ratio with incidence is much smaller.

The present tests are preliminary ones in a programme aimed at obtaining a fuller understanding of the flow about lifting vehicles at high supersonic speeds.

LIST OF CONTENTS

---

1. *Introduction.*

In recent years interest has grown in the performance of lifting vehicles capable of sustained and manoeuvring flight at hypersonic and high supersonic speeds. Various shapes have been suggested for these vehicles and a considerable amount of wind-tunnel testing has been carried out, mainly in the U.S.A. In only a few cases, however, has a detailed study been made of the flow on and about the vehicle, and this type of information is urgently required if a full understanding of the aerodynamic behaviour is to be obtained.

As a preliminary step in a programme for studying lifting bodies at high supersonic speeds, tests have been made on two simple delta wings at a stream Mach number of 4·03. The wings were tested both alone and in combination with a family of half-cone bodies mounted on their lower surfaces. This type of vehicle was chosen because of the simple geometric shape of both components and the relatively simple form of the associated flow fields. It is the interaction of these flow fields which is of prime interest in the present investigation. The use of delta-wing and half-cone combinations in the present context should not be taken to imply that these represent the best aerodynamic design for flight at high supersonic speeds.

2. *Experimental Details.*

   2.1. *The Models.*

Two wings were tested, one having a leading-edge sweep of 80° and the other a sweep of 75°. It is more convenient to designate these wings by means of ε, the semi-vertex angle of the wing planform, i.e., the complement of the sweepback angle. The angle ε thus has two values, 10° and 15°, and the corresponding planforms are shown in the upper parts of Figs. 1a and b. The centreline chord (c) of both models was 5 in., and the aspect ratios were 0·705 and 1·072 respectively.

The cross-section of each wing was triangular, and the angle between the flat undersurface and the upper-surface ridge-line was 5° in both cases, giving a maximum thickness at the base of 0·4375 in. The disposition of surface pressure holes is shown in Figs. 1a and b; these were grouped along rays passing through the vertex, the angle between the centreline and the ray being denoted by θ. Pressure holes were sited at four chordwise positions, corresponding to values of x/c of 0·4, 0·6, 0·8 and 0·95, both on the upper and lower surface. Because it corresponds to the ridge, there were no upper-surface holes at $\theta = 0°$. Only a limited number of pressure tubes could be accommodated in the model, and so several holes were connected to a common tube; holes not required were sealed off with a mixture of celluloid dissolved in acetone.

2

The wing models were designed so that 5 in. long half-cone bodies could be rigidly attached to their undersurfaces. The semi-vertex angles (ξ) of these half-cones varied between $4°$ and $13°$ (*see* Figs. 1a and b), thus enabling progressively more of the wing lower surface to be covered up by the body. For the combination with $\varepsilon = 10°$, $\xi = 10°$ (abbreviated to $10°/10°$ subsequently in the text) all the wing lower surface was covered. The half-cones had pressure holes distributed around their periphery, at radial angles (ϕ) of $15°$, $45°$, $60°$ and $90°$ and at the same values of x/c as the wing holes. Each body pressure tube was connected to two body holes in forward and aft pairs along each radial line and those not required were sealed off. The slide elevation of the wing, alone, and in combination with the bodies, is illustrated in Fig. 1c.

All the models were supported from the rear by a sting attached to the incidence gear of the tunnel, the sting also being used to support the pressure tubes passing out from the rear of the model. No artificial means was used to cause boundary-layer transition on the model surfaces.

2.2. *The Tunnel and Test Conditions.*

All the tests were run in the N.P.L. 7 in. $\times$ $4\frac{1}{2}$ in. blowdown wind tunnel at a nominal Mach number of 4, a stagnation pressure (H_0) of 75 p.s.i.a., and a stagnation temperature of approximately $280°K$; slight day-to-day variations occurred in this last quantity.

The combinations with $\varepsilon = 10°$ were tested in the normal model position; surveys with a slender pressure-plotting circular calibration cone showed that the Mach number along the length of the model when this was at zero incidence varied between $4·02$ and $4·04$; a mean value of $4·03$ was therefore used in reducing the observations. For the combinations with $\varepsilon = 15°$, tested subsequently, a more forward station in the tunnel was used. Unfortunately the flow in this region was less uniform than for the original position, the local Mach number falling from about $4·07$ at the model apex to $4·02$ at the base. A mean Mach number of $4·03$ was still used in the calculation and a correction applied to the pressures measured at the two most forward hole positions.

The variation of tunnel pressure, and hence free-stream Mach number, for both model positions is shown as broken lines in Figs. 2a and b.

Based on the 5 in. centreline chord, a stream Mach number of $4·03$, 75 p.s.i.a. stagnation pressure and $280°K$ stagnation temperature, the test Reynolds number is $3·4$ million. The Mach angle for a Mach number of $4·03$ is $14·37°$. The leading edge of the $10°$ wing is therefore 'subsonic', whilst that of the $15°$ wing is just 'supersonic'.

2.3. *Experimental Procedure.*

The wing-body combinations with $\varepsilon = 10°$ were tested first, the upper- and lower-surface pressures on the wing alone being recorded initially, using a multitube barometer-type mercury manometer. Subsequently the $10°/4°$, $10°/6·7°$ and $10°/10°$ combinations were tested, pressures on the cone surface and exposed wing undersurface being obtained. A few check readings of the wing upper-surface pressure were taken when some lower-surface bodies were in position. Because several holes were connected to a single pressure outlet at least four runs were required at a given incidence to obtain a complete distribution of pressure on one surface.

The model incidence was varied in nominal steps of one degree between $0°$ and $8°$. Zero incidence corresponded to the condition where the lower surface of the wing was aligned with the undisturbed stream. Because of the aerodynamic loads imposed on the model and sting the true aerodynamic incidence was somewhat greater than the nominal value; this correction was found by observing the model during a tunnel run with a telescope and also by using weights to simulate the aerodynamic loads when the tunnel was shut down, the change in attitude then being measured with an inclinometer. For the $\varepsilon = 10°$ wing alone, a nominal incidence of $8·0°$ becomes a corrected incidence of $8·1°$, which increases to $8·2°$ for the $10°/10°$ combination.

A similar procedure was used for the model having $\varepsilon = 15°$, the wing alone, and the $15°/4°$, $15°/10°$ and $15°/13°$ combinations being tested. In this part of the test, due to lack of time, no results were taken at a nominal incidence of $3°$ on the $15°/4°$ model, neither were data obtained at the chordwise stations $x/c = 0·4$ and $0·8$. A $15°/6·7°$ model was available for test, but was not used.

3

Because of the less rigid mounting associated with the forward model position, and the larger model area, the corrections to nominal incidence for the 15° models are rather larger than in the earlier tests on the 10° family, and now consist of two parts. One is a fixed correction to nominal value set on the incidence gear; this is 0·8° for the wing alone, 15°/4° and 15°/13° models, and 0·1° for the 15°/10° combination. The second correction is due to the aerodynamic loading; this amounts to 0·3° at 8·0° nominal incidence for the wing alone and, in the worst case, 0·8° for the 15°/13° combination at the same nominal incidence.

Schlieren flow photographs were obtained for each combination for the entire incidence range and in addition, photographs of several oil-flow patterns were taken, principally of the lower-surface flow when the bodies were present, and of the upper-surface flow for the wing alone.

The tests were carried out at intervals between October, 1961 and March, 1963. The long time-span of the experiments was due mainly to the installation nearby of a new blowdown tunnel, which caused the 7 in. $\times$ $4\frac{1}{2}$ in. tunnel to be out of action from time to time.

3. Results.

3.1. Surface Pressure Distributions.

3.1.1. Conical nature of flow.

One of the principal reasons for having four chordwise pressure-hole stations was a hope that this would provide information on the conicity of the flow about the models. If the flow field is conical (as inviscid theory would predict) then the surface pressures should vary only with the ray angle θ and be independent of x/c.

The variation of pressure along the undersurface midchord line ($\theta = 0°$) for the two wings alone is shown in Figs. 2a and b. The scatter of the results is disappointingly large. Errors in pressure readings may well arise from the complex sealing operations necessary because several pressure holes were connected to one pressure outlet. Though great care was taken to ensure that leaks between adjacent holes were minimised (checks were made before and after every run), very small leaks had sometimes to be accepted. Errors might also arise from imperfections in the shape of the holes themselves, due perhaps to sealing material adhering to the hole edge.

Variations in tunnel static pressure along the model length may also contribute to the general scatter, but this is felt to be a smaller effect, particularly for the 10° wing, where the changes in tunnel flow indicated by the calibration cone are quite small (see Fig. 2a). A static survey with such a cone is admittedly not the best way of finding the static-pressure changes within a given volume of the tunnel working section; however, the measured variation seems often to be opposite to the pressure trends obtained with the calibration cone, and persists as incidence is applied to the model. In general small disturbances in the tunnel flow are likely to propagate downstream from all four walls and vertical movement of the model through the application of incidence should then disturb the form of the scatter. This does not occur and it is possible that the scatter as such is associated with pressure-hole imperfections. In addition, however, there appears to be a longitudinal pressure gradient, such that the Mach number falls with increasing x/c, and this gradient is not greatly affected by model attitude.

As was pointed out in Section 2.2 the tunnel flow is less satisfactory at the forward model-position used for tests on the 15° combination; the tunnel calibration is shown as a broken line at the bottom of Fig. 2b. The stream Mach number appropriate for the two forward pressure-plotting stations ($x/c = 0·4$, 0·6) is about 4·07 instead of the value 4·03 assumed in the analysis. Accordingly all the data presented in the present text for the 15° models at these stations has been corrected to allow for this change in free-stream Mach number; the correction has been assumed to apply unchanged over the complete incidence range. Once again, the data appear to be scattered about some mean pressure gradient, whose sign is similar to that of Fig. 2a. This pressure gradient is perhaps the most striking feature of Figs. 2a and b and if tunnel pressure variation is excluded, it seems most likely to be associated with the boundary-layer growth along the surface. Oil-flow patterns indicated that the boundary-layer was turbulent at all incidences. In general one might expect a growing boundary-layer on a plane surface to cause a longitudinal increase in Mach number (cf. viscous-interaction effects at hypersonic speeds). The present trend is the

opposite of this, and hence may arise from three-dimensional effects on the boundary-layer development,* which make the effective shape of the lower surface non-planar. Even this argument must perhaps be restricted to higher supersonic speeds.

Similar gradients of varying magnitude are present on the $10°$ wing undersurface away from the centreline. For example, in Fig. 3 the pressure distributions for the ray $\theta = 8.5°$ are presented. Since this ray lies close to the wing leading edge (i.e. $\theta = 10°$) the presence of gradients may be at first sight unexpected; however, it is possible that small spanwise effects on the lower surface may induce slightly higher pressures over the rear of the model near the tips, particularly at the higher incidences. There is also a marked increase in pressure gradient with model incidence for the results shown in Fig. 3. Once again the surface flow departs slightly from the ideal conical type.

At other ray angles on the $10°$ wing undersurface the pressure gradients are intermediate between those shown in Figs. 2a and 3. For the $15°$ wing, along rays away from the centreline, changes of pressure occur which are similar to those on the $10°$ wing, though because of the rather higher scatter of the results, the trends are less well defined. On both model upper surfaces, chordwise pressure gradients were also present at low incidences** and were of similar magnitude to those on the lower surface.

The departures from true conical flow discussed in the preceding paragraphs are fortunately small enough to allow most of the analysis to be performed at only one typical chordwise station on each model without great loss in accuracy, but with considerable economy in presentation. For the remainder of the report, most attention will be given to the chordwise stations $x/c = 0.4$ and 0.6, with occasional references to other chordwise stations to indicate the magnitude of the differences likely to exist between different positions. Finally, it should perhaps be pointed out that at no stage in the investigation was any effect obtained at $x/c = 0.95$ which could be attributed directly or indirectly to the closeness of the hole to the base of the model. It is assumed, therefore, that upstream effects from the blunt base do not penetrate along the model surface as far as this pressure-hole position.

3.1.2. *Spanwise pressure distributions on lower surface.*

At a single chordwise station ($x/c = 0.4$) the spanwise pressure distributions for the family of models having $\varepsilon = 10°$ are given in Figs. 4a to d. Similar distributions, at $x/c = 0.6$, for the $15°$ set of models, appear as Figs. 5a to d.

Consider first the results for the wings alone (Figs. 4a, 5a). The pressure falls towards the tip at zero incidence for $\varepsilon = 10°$ and, less markedly, on the $15°$ wing at $\alpha = 0.8°$. A similar effect occurs in the results presented in Ref. 1 for a wing with $\varepsilon = 18.4°$ at $M_0 = 3.97$. The spanwise pressure variation may well be due to a non-uniform boundary-layer thickness across the span, which effectively modifies the shape of the flat undersurface and perhaps causes the chordwise pressure gradients discussed in Section 3.1.1; moreover, the shock from the apex may not be exactly conical for a body of triangular cross-section and may be slightly weaker in the vicinity of the wing tips. At higher incidences the pressure rises towards the tips, a trend which would be expected from linear flat-plate supersonic theory. The value of this theory in predicting the surface pressures is rather limited however. In Fig. 6a the centreline pressures are plotted against incidence for $\varepsilon = 10°$; the curve is non-linear and only near zero incidence does its slope agree with that predicted by linear theory. As might be expected both the linear and exact theories for a two-dimensional wedge predict higher pressures than are observed. The simple Newtonian theory gives about the right trend at high incidence, but the pressure levels are incorrect. The measured pressures

---

*Oil-flow patterns obtained on this wing (and on the $15°$ wing) show a slight general spanwise drift of the surface streamlines particularly at the higher incidences. Near the leading edge, however, there is an inward deflection of the streamlines, which soon straighten to flow almost parallel to the undisturbed stream.

**That is for incidences below $5°$, where the upper surface acts as a compression surface. Above this incidence, the leading-edge effects (including flow separation) begin to dominate the flow.

at the centreline on both wings agree very well provided the comparison is made at the same value of x/c, as in the lower part of Fig. 6b, where $x/c = 0.6$. The centreline pressures are clearly independent of ε for the present wings.

Despite its failure to predict the centreline pressures, it seems worth while considering whether linear flat-plate theory correctly estimates the spanwise variation. The broken curves of Fig. 4a are obtained from this theory, with the pressure level displaced so that the curves pass through the experimental values at $\eta = 0°$. Close to the leading edge, the predicted rapid rise in pressure is, not unexpectedly, absent, but over most of the wing surface the spanwise pressure trends are in reasonable agreement with the theory.

The effect of adding a series of increasingly large conical half-bodies to the 10° wing undersurface is shown in Figs. 4b, c and d. In the last of these, the body covers the entire lower surface and the flow approximates closely to that on the windward side of an isolated cone. For the smallest body (Fig. 4b), the most noticeable effect of the added volume is the general rise in the overall pressure level on the model undersurface. The changes in the shape of the pressure distribution within the region occupied by the cone, though well-defined, are less marked than might have been anticipated. The pressure fall towards the wing tip at zero incidence is accentuated by the presence of the body; once more it is uncertain whether this is principally due to an additional distortion of the bow shock wave or to increased spanwise drift of the boundary layer. With the large bodies the pressure distributions become more and more distorted from those observed on the plain wing, until for the 10°/10° model the cone flow is completely dominant. Corresponding results for the 15° combinations are included as Figs. 5b, c and d.

It is convenient at this stage to consider the influence of the surrounding wing on the flow over the cone. The opposite effect, the modification of the wing flow by the cone, will be discussed later.

The variation of the surface pressure on the most windward cone generator ($\phi = 90°$) with model incidence is plotted in the upper part of Fig. 6b for the $\xi = 4°$ cone in combination with both wings. The two sets of results are in good agreement. At zero incidence, the cone-surface pressure ratio is slightly above that for a 4° half-angle cone in inviscid flow at $M_0 = 4.03$ and the small difference may reasonably be attributed to boundary-layer growth on the cone surface, which increases the effective cone angle. The subsequent variation in pressure at this position with incidence is quite well predicted by a tangent-cone approximation; i.e. it is assumed that the $\phi = 90°$ generator behaves as if it were part of a cone of semi-angle $(\xi + \alpha)$ at zero incidence. A similar plot for the pressures at $\phi = 90°$ on the 10° cone, with both the 10° and 15° wings, is given in Fig. 6c. Once again the two sets of results agree and since those from the 10°/10° combination are effectively obtained with an isolated cone, it seems fair to conclude that the exposed wing on the 15°/10° model has little influence on the cone pressures at $\phi = 90°$. As in Fig. 6b, the surface pressures are predicted reasonably well by a tangent-cone approximation. An alternative approach is to determine the pressure for the zone at zero incidence from cone tables, and use simple Newtonian theory to predict the subsequent change in pressure with incidence. This gives a closer approximation to the observed pressures than tangent-cone theory (Fig. 6c); Newtonian theory alone underestimates the zero-incidence pressure level (Fig. 6b).

The circumferential pressure distributions for the 10° cone fitted to the 10° wing (Fig. 4d) are similar in shape to those obtained elsewhere for complete circular cones at incidence (see, for example, Refs. 2 and 3). These results may of course be compared with theoretical data for slender cones at incidence (M.I.T. tables[5], for example), but in the present context we are more concerned with considering how the cone pressures away from $\phi = 90°$ are influenced by the adjacent wing surface. A simple reference curve for the circumferential pressure variation is given by the Newtonian theory; the pressure coefficient on the surface may be related to the local surface incidence β. For a cone of half-angle ξ, at an incidence α with respect to the stream[2,3]

$$\sin \beta = \sin \xi \cos \alpha + \cos \xi \sin \alpha \sin \phi.$$

Then
$$\frac{(C_p)_\phi}{(C_p)_{\phi=90°}} = \sin^2\beta,$$

6

or in terms of the present pressure ratio p/H_0, at a stream Mach number of 4·03,

$$\left(\frac{p}{H_0}\right)_{\phi} = 0\cdot00633 \left[\left(\frac{p}{H_0}\right)_{\phi=90^{\circ}} - 0\cdot00633\right] \sin^2\beta,$$

where the theoretical and experimental values are made to agree along the most windward generator, $\phi = 90^{\circ}$.

Newtonian-theory curves for the 10° wing are given in Fig. 4d for two incidences, and it will be seen that the theory predicts too high pressures for $\phi < 60^{\circ}$. No improvement results from using equivalent cone theory, i.e. assuming that the pressure on the model surface with local inclination β is identical with that on a circular cone of half-angle β at zero incidence. Similar differences between theory and experiment were observed by Peckham and reported in Ref. 3; this paper contains a full discussion of the relative merits of the above theories (and others) for estimating surface pressures on cones at high supersonic speeds.

Turning now to the pressure distributions obtained on the 15° wing with a 13° cone-body (Fig. 5d) it will be seen that the Newtonian theory now gives pressures which are *lower* than those observed on the model and it seems reasonable to attribute this change to the distortion of the cone flow by the small exposed wing surface. The effect of the wing therefore is to increase the cone-surface pressures in the vicinity of the wing-body junction.

It may be argued of course that the cone on the 10°/10° model is not truly representative of an isolated complete circular cone, and it is true that direct comparison of the present results with those for a similar complete cone at the same Mach number is not possible. The validity of the present assumption can be demonstrated sufficiently well by means of Fig. 7 however. Here the ratio of the pressure coefficients at $\phi = 15^{\circ}$ and 90° is plotted against model incidence for isolated cones with semi-apex angles of 5°, 10° and 15°, and for stream Mach numbers between 2·91 and 6·85 (Refs. 2–4, 6). The influence of Mach number on this pressure ratio seems to be very small, as might be expected from cross-flow considerations. The data obtained from the present 10°/10° model fit in very well with the isolated cone results. Similar agreement may be obtained at $\phi = 45^{\circ}$, and it seems clear that the model upper surface has little effect on the lower-surface pressures, even though the leading edge of the combination is subsonic in type.

In contrast, the pressure-ratio curve for the 15°/13° model, also shown in Fig. 7, does not conform to the general pattern, the pressure level at the $\phi = 15^{\circ}$ station being much higher. Presumably the small region of exposed wing acts as a spoiler or strake to the cross-flow and significantly increases the cone-surface pressures near the junction. An alternative method of showing this pressure rise is illustrated in Fig. 8 where data from the 10°/10° and 10°/15° models are used. In Fig. 8b, with $\phi = 15^{\circ}$, there is a large difference between the curves for the two models, which may be attributed to wing influence. This influence is smaller at $\phi = 45^{\circ}$ (Fig. 8a), and as Fig. 6c shows, it disappears at $\phi = 90^{\circ}$.

One may pursue this matter a little further by considering whether the observed cone pressures near the junction are simply the superposition of the wing field on the cone flow. That is, the total pressure change from the free-stream value, p_0, may be written as the sum of two component pressure changes

$$\left(\frac{p}{H_0} - \frac{p_0}{H_0}\right)_{WB} = \delta\left(\frac{p}{H_0}\right)_{WB} = \delta\left(\frac{p}{H_0}\right)_{W} + \delta\left(\frac{p}{H_0}\right)_{B}$$

where the suffices WB, W and B signify the wing-body model, and the wing and body alone. By adding p_0/H to both sides this may be rewritten in two forms:

$$\left(\frac{p}{H_0}\right)_{WB} = \left(\frac{p}{H_0}\right)_{B} + \left(\frac{p}{H_0} - \frac{p_0}{H_0}\right)_{W} \tag{1a}$$

$$= \left(\frac{p}{H_0}\right)_{W} + \left(\frac{p}{H_0} - \frac{p_0}{H_0}\right)_{B}. \tag{1b}$$

7

The predicted wing-body pressure may be found, using equation (1a), by adding to the full-line curves $(p/H_0)_B$ of Fig. 8, the difference between the wing-alone pressures (Fig. 5a) and free-stream pressure. These simple predictions are plotted as broken lines in Fig. 8. Reasonable agreement is obtained at $\phi = 15°$ where the body pressure hole lies close to the wing surface. For $\phi = 45°$, the actual pressure hole is some distance from the wing surface and an attenuation of the wing field must be expected. Indeed the simple superposition theory overestimates the cone-surface pressures, but this reduction in wing influence probably arises less from the normal decrease in the wing field with distance as from the increasing independence of the blunt-body cross-flow from the geometry of the upper half of the model.

From information of this type it is possible of course to derive an influence factor, F, dependent mainly on ϕ, which could be used to modify equation (1a), e.g.

$$\left(\frac{p}{H_0}\right)_{WB} = \left(\frac{p}{H_0}\right)_B + F\left(\frac{p}{H_0} - \frac{p_0}{H_0}\right)_W. \tag{1c}$$

At an incidence of 4°, for example, F would be about unity at $\phi = 15°$, and about 0·3 for $\phi = 45°$ (Fig. 8). In addition, Fig. 6c suggests that F may be taken as approximately zero at $\phi = 90°$. A similar analysis to that contained in Fig. 8, but for $\phi = 60°$, indicates that F then has a value near 0·2. These four points are plotted as circles in Fig. 9.

Further data of this type can only be obtained indirectly because of the absence in the present tests of information on the values of p_B for cones other than that with $\zeta = 10°$. A little progress can be made, however, provided the uncertainties involved are borne in mind. Using Fig. 7, it is possible to estimate pressure-ratio curves for isolated cones of half-angle 4° and 6·7°, and then use these to deduce F at $\phi = 15°$. A similar analysis may be made at other values of ϕ, and points obtained in this way are shown as crosses and triangles in Fig. 9. The mean curve shown in this Figure is only intended to illustrate the general trend, and in view of the uncertainties inherent in determining F and the limited amount of analysis that has been undertaken, it should be made clear that the main purpose of this Figure is to draw attention to a possible way of regarding the field interaction.

Before leaving this aspect of the analysis, it is of interest to note that the surface pressures on the most slender cone ($\zeta = 4°$) are independent of ε as is shown for the two most extreme pressure-plotting stations in Fig. 6b ($\phi = 90°$) and Fig. 10 ($\phi = 15°$). At the plan position subsequently occupied by the body hole at $\phi = 15°$, the pressures on the isolated wings are very similar and both sets correspond closely to the broken line in Fig. 10. In this case equation (1b) may be used and the isolated-cone pressure increment deduced from Fig. 7. The result is the chain-dotted line which lies close to the experimental observations for the wing-body combination, and over the incidence range the value of F is a little above unity. The value at $\alpha = 4°$ plotted in Fig. 9 was derived by using equation (1a), but this gives identical results.

3.1.3. Spanwise pressure-increment distributions on lower surface.

In the preceding section there was some discussion of the validity of considering the observed pressure field as being the sum of the pressure field due to one component of the combination (say, the body) and the pressure increment due to the influence of the other component (the wing). Some assessment could be made in this way of the influence of the wing on the cone field. Of more practical importance is the changes that the presence of the cone causes to the wing-alone surface pressure distribution, particularly on the lower surface. Pressure changes due to the cone may then be related directly to changes in the lower-surface contribution to the lift or pressure drag of the combination. From this viewpoint it is convenient to replot the present data in terms of an alternative form of pressure increment $\Delta (p/H_0)$ where for a given station

$$\Delta\left(\frac{p}{H_0}\right) = \left(\frac{p}{H_0}\right)_{WB} - \left(\frac{p}{H_0}\right)_W.$$

$\Delta (p/H_0)$ is therefore a measure of the local cone-induced pressure change. For stations on the exposed

8

wing surface it may be obtained directly by subtracting the observed pressure level at a given hole for the wing alone from its reading when the body is present. For the part of the span covered by the body the spanwise positions of the body and wing holes do not correspond; it is necessary therefore to interpolate to find the wing-alone pressure for a particular body-hole position.

These body-induced pressure changes (or spanwise load increments) are presented in Fig. 11 for combinations with $\varepsilon = 10°$ and in Fig. 12 for those with a wing of 15° half angle. The pressure increments occurring on the part-span occupied by the body arise, of course, from the physical displacement of the solid surface in that region. Outboard of the cone, the pressure changes are due to the imposition of the body flow field.

The effect of model incidence on the spanwise load increments are most marked near the body centre-line ($\phi = 90°$) where there is a rapid change in pressure as the incidence increases. On the cone surface near the junction ($\phi = 0°$) the loading decreases with rising incidence for all models except those with $\zeta = 4°$, where, however, the pressure changes are small and in consequence may be influenced by the experimental scatter. If the reversal in trend is accepted as real, it might be due to boundary-layer growth in the junction which causes an effective distortion of the conical body shape. This explanation must remain conjectural because the oil-flow patterns provide no worthwhile supporting evidence.

The loadings induced on the wings by the 4° body are, as would be expected, small and change little with increasing incidence. Once again the experimental scatter precludes any decision as to whether the opposite trend with incidence in Figs. 11a and 12a is real. On the 15°/4° model the induced loading increases with incidence and seems well established, but this effect is the opposite of that apparent on the 10°/6·7° and 15°/10° combinations. The simplest explanation seems to be in linking the body-induced changes with incidence on the wing with those on the body near the junction. Considered this way the results are reasonably consistent, though the difference between the small and large cone results near the junction still requires consideration, as was mentioned in the preceding paragraph.

Another feature of the wing pressure-increment curves is the decrease in induced loading towards the tips, an effect which would be expected from a natural decay with distance of the body influence. This spanwise diminution of loading is most well-defined for the 4° bodies, is apparent for the 6·7° body at the higher incidences, and can only be assumed in the curves for the 15°/10° model. The *increase* in loading towards the tip at low incidence on the 10°/6·7° combination (Fig. 11b) is not readily explained. It is apparent at all four chordwise stations (results at $x/c = 0·4$ and 0·95 are plotted in Fig. 11b) and thus would seem to be unconnected with local hole defects or tunnel flows. Boundary-layer growth in the junction, on the evidence of the oil-flow patterns, is not especially significant in this case, and at present the reason for this effect is unknown. On a more careful, subsequent investigation, in which the overall accuracy is higher than in the present experiment, it might be rewarding to study the small differences in pressure increments close to the junction on the wing and on the body. In the present tests, these do not match as well as one would like.

Since the pressure increments on the exposed wing area are basically due to the presence of the conical underbody, it is possible in some cases to compare the experimental loadings with those deduced from simple theory. Such an analysis can be made readily only for 0° incidence, when the plane of the wing undersurface coincides with the stream direction. The flow field about cones of the required semi-vertex angles can be found by graphical interpolation of the various parts of Fig. D2 in Ref. 10. These contain the Mach number increment with increasing distance from specified cone surfaces, and by assuming that there is no total pressure loss through the shock, the associated pressure change can easily be found. These pressure increments are plotted as full lines in terms of the angle θ in Fig. 13a for the cones with $\zeta = 4°$, 6·7° and 10°, at a stream Mach number of 4·03. The experimental values agree well with the theoretical curves for the 4° and 10° cones and reproduce the theoretically-predicted decrease in body influence towards the tip of the wing. The two points for $\zeta = 6·7°$ show the reverse trend, as was pointed out earlier. For $\zeta = 4°$, the induced loading is largely independent of wing angle ε and this part of Fig. 13a is reproduced again in the lower section of Fig. 13b. The upper part of the latter Figure shows similar experimental results at 8·1° incidence and these are also in good agreement with the theoretical line for zero cone incidence showing, as Fig. 11a does, that the wing incremental pressures are insensitive to incidence on this model. Moreover, even at $\alpha = 8·1°$, the induced loading is largely independent of ε.

9

A simple theoretical estimate may also be made of the cone's influence at zero incidence through slender-body theory. Assuming C_p to be equal to $-2u/V$,* where u is the streamwise perturbation velocity and V is the stream velocity, then it can be shown that the pressure coefficient increment (ΔC_p) induced by a cone of half angle ζ under a sonic-edged** delta wing is

$$\Delta C_p = 2 \tan^2 \zeta \cosh^{-1} \left(\frac{\cot \theta}{B} \right) \qquad (2)$$

where $B = \sqrt{(M_0^2 - 1)}$ and θ is the ray angle. At a Mach number of 4·03, the pressure increment is given by

$$\Delta \left(\frac{p}{H_0} \right) = 0·00633 + 0·0720 \, (\Delta C_p). \qquad (2a)$$

This increment has been evaluated for all three cone angles and is plotted in Fig. 13a, though the slender-body theory might be expected to be valid only for the most slender cone with the 15° wing. For this body, $\zeta = 4°$, the agreement between the slender-body and exact-cone theory is good, if the uncertainties of the graphical processes of obtaining the latter are borne in mind. Moreover, the slender-body theory, derived for a sonic-edged wing is seen to apply equally well to the $\varepsilon = 10°$ wing with a subsonic leading edge. For larger values of ζ, exact-cone theory appears to be necessary. Ref. 15 shows that even if linearised theory is used with the boundary conditions satisfied on the cone surface (instead of on the axis, as in slender-body theory) little improvement results.

Savin[7] has developed a simplified theory for predicting flow fields about certain classes of wing-body combinations (including the present families) at hypersonic speeds and small angles of attack, but his theory is only applicable at the present stream Mach number (4·03) for larger ratios of ε/ζ than were used in the tests being described. No comparison between this theory and experiment is therefore possible in the present text.

3.1.4. Uper-surface flow.

In the previous sections, only the lower-surface flow has been discussed in detail and it now seems appropriate to consider briefly the upper-surface pressures and flow. The complete surface pressure distributions on both wings are plotted in Figs. 14a and b, those for the upper surface being drawn as full lines. Because of the absence of pressure holes outboard of $\theta = 8·5°$ and 12° respectively on the two wings, and the few pressure holes which are available to cover the remaining surface, considerable uncertainty exists about distribution shape; the curves presented, drawn with the aid of the oil-flow photographs, are, however, reasonably consistent with other data for slender delta wings.

For $\varepsilon = 10°$, and with increasing incidence, the upper-surface suction peak builds rapidly near the leading edge; flow separation then occurs, but with the pressure still falling beneath an increasingly strong vortex. Finally, as the vortex moves inboard and away from the wing surface the pressure in the leading-edge region falls more slowly.

An example of the influence of the separated-flow development on the pressure at a selected hole on each of the two isolated wings is given in Fig. 15a; both holes lie near the leading edge. The movement of the reattachment line, deduced from oil patterns is shown in Fig. 15b, and this Figure suggests that on the 10° wing a pressure hole at $\theta = 8·5°$ ($\eta = 0·846$) should begin to respond to the vortex at an incidence (α_k) of close to 3·0°. An analogous event, A , on the 15° wing occurs for $\alpha_k = 5·8°$. In Fig. 15a, event A is seen to correspond to the onset of the rapid pressure fall. Event B in Fig. 15b is the rapid retardation

---

*For a discussion of the relative merits of using the linear and non-linear forms of the equation for C_p, see Ref. 15.

**At $M_0 = 4·03$, a sonic-edged wing would have $\varepsilon = 14·37°$. For the 15° wing then this approximation is reasonably valid.

of the inboard vortex movement, and is related to the second kink in the pressure curves. Presumably at this stage the vortex pair moves away from the wing surface; such a motion cannot be detected with certainty from surface oil-patterns alone.

We will next consider the influence of the underslung half-cone bodies on the upper-surface flow. In Fig. 15c, the pressures at $x/c = 0.6$, $\theta = 8.5°$ are plotted against incidence for the 10° wing when alone, and when in combination with a 10° half-cone. Even at zero incidence the half-cone causes a reduction in upper-surface pressure, and this effect is most marked for incidences between 1° and 5°. In the light of the discussion on Fig. 15a, the change of shape of the pressure curve due to the body can be attributed to alteration in the development of the vortex flow above and on the model. The vortex pattern would seem to develop at an earlier incidence,* but this point cannot be checked directly because no oil patterns were obtained on the upper surface of the 10°/10° model. A comparison can be made, however, between the 15°/0° and 15°/13° models at a few incidences. There is a noticeable difference in the upper-surface flow. At $\alpha = 9.6°$, there is a strong secondary separation at about 0.65 semispan on the 15°/13° combination; when the underbody is absent the flow remains attached up to the leading edge. At a lower incidence ($\alpha \simeq 7°$) this feature still exists, but the vortex is far more marked when there is a body (Fig. 16). Even if allowance is made for the rather poor quality of the oil patterns in these two cases, it is clear that the streamline curvature under the vortex is higher for the 15°/13° model, indicating a more developed vortex or at least one which is closer to the surface. The 15°/13° model, it should be noted, is at a somewhat lower incidence than the wing alone. The actual reattachment positions for the model with body are plotted in Fig. 15b and agree well with those taken for the 15° wing alone; the differences evident in Fig. 16 may be attributed mainly then to the vortex strength and position above the surface. Similar differences of pattern, if pertinent to the 10° models, might explain the changes shown in Fig. 15c.

Because of lack of tunnel time, upper-surface pressure was measured only on the wings alone and on the 10°/10° combination for the test incidence range, and in addition at 0° and 8.1° on the 10°/6.7° model. For the last model at the lower incidence, the surface pressure at $\theta = 8.5°$ lies between those observed on the two other models (Fig. 15c). This result conflicts with an obvious possibility that at zero incidence the upper-surface pressure should rise as a result of the stronger bow shock associated with the presence of the body. At 8.1°, the pressure level for the intermediate model is close to that obtained on the wing alone.

The foregoing evidence, admittedly scanty, suggests that the effect of a lower-surface body on the upper-surface pressures is small, provided the body is not too large. If the body is big compared with the wing there may be a change in the development of the separated flow, and associated surface-pressure variations. Presumably as the body-wing junction approaches the leading edge, the cross-flow towards that edge changes, affecting the angle at which the flow finally separates. This in turn alters the vortex position and the upper-surface pressures.

3.2. Bow Shock Wave.

Schlieren photographs were taken for the 10° combinations over the complete incidence range, and hence it is possible to determine how the angle between the lower-surface bow-wave visible in the photographs (i.e. at $\phi = 90°$) and the stream direction various with cone angle ξ and incidence α. This shock angle λ is plotted in Fig. 17 for all three body semi-vertex angles, and the measured values agree well with data deduced from Ref. 7 for the same values of ξ. The variation of λ with incidence is a little less than that predicted by assuming that the shock from the cone at incidence is identical with that produced by an isolated cone at zero incidence having a semi-vertex angle of $\xi + \alpha$. On this evidence one would expect that at the higher incidences the surface pressures along the generator $\phi = 90°$ should be rather lower than those given by tangent-cone theory. Figs. 6b and c show that this is the case and relative slopes of the theoretical and experimental results in Fig. 17 correspond well with those in Figs. 6b and c.

---

*The absence of data for the 10°/10° model at 1° incidence is unfortunate in this context.

3.3. *Model Forces.*

The overall normal force, and hence the lift, on the two isolated wings may be derived by integrating the spanwise pressure distributions of Figs. 14a and b. These lift results, reduced to coefficient form C_{LW} are contained in Fig. 18. For the 10° wing, the integration was carried out at all four chordwise stations for several incidences; the scatter is very small (having regard to the uncertainties in drawing the actual distributions) and a single mean line may be drawn through all the points. In the case of the larger wing the integration was performed only for $x/c = 0.6$ and 0.8; again the differences are small.

Zero lift occurs at a model incidence near 2·5° for both wings, i.e. when the upper and lower surfaces are at almost the same inclinations to the stream direction. In the region near zero lift, the experimental lift-curve slope lies very close to that predicted by linear flat-plate theory. This good agreement is to some extent fortuitous, and arises partly from the cancellation of disagreements between theory and experiment near the centreline (Fig. 6b for example) and near the leading edge. The influence of the leading-edge separation should become apparent in the lift curves once it extends to the most outboard pressure hole, that is, event A of Fig. 15, which has been transferred to both sections of Fig. 18. For $\varepsilon = 10°$ it is apparent that the non-linear part of the lift arises after event A . As the vortices cease to move rapidly inboard (event B), the non-linear lift grows less quickly. For the 15° wing, which has an almost-sonic leading edge, the non-linear lift is very small, but is just detectable at the higher incidences.

By integrating the lower-surface spanwise loading-increment curves of Figs. 11 and 12, the lift induced on the lower surface due to the presence of the body may be found; in doing this it is convenient to keep separate the contributions from the body surface and exposed wing surface. In general the loading curves on the body are reasonably well defined though for $\xi = 4°$, the incremental pressures are small ·and affected by the observational scatter. On the wing surface it is necessary to extrapolate the curves out to the wing tip in all cases using the shape of the theoretical curves (Fig. 13, for example) as a general guide. The curves for the 10°/6·7° model are particulary difficult in this respect. On the 15°/10° combination, there are only two closely-spaced holes on the exposed wing surface (Fig. 12b) and theory is here most helpful in drawing the most likely curve. Finally, for the 15°/13° model (Fig. 12c) there are no pressure holes on the exposed wing and the wing contribution to the induced lift cannot be assessed directly.

The foregoing remarks on the limitations of the experimental data should be kept in mind during the subsequent discussion since it is clear that the induced forces on the models can only be found in an approximate manner. Moreover, the small change in the upper-surface lift due to the presence of a lower-surface body has been deliberately neglected, because there is insufficient data to allow a proper estimation to be made. Nevertheless, it is felt that the general conclusions and trends which result are valid and afford some insight into the behaviour of wing and half-cone combinations.

The lower-surface lift increments are presented in coefficient form in Figs. 19 and 20 for the 10° and 15° wings, respectively, the body and wing contributions being given separately where appropriate. The curves for the combination with $\varepsilon = 10°$ are similar in general shape but with changes in the relative magnitudes of the body and wing contributions. The most noticeable features are the reduction in wing lift increment with rising incidence, and at the same time the growth of the body contribution. As a result the total induced-lift curve tends to have a minimum at an incidence which decreases as the body grows in size. The actual change in ΔC_L with incidence is quite small and the large vertical scales of Figs. 19 and 20 should be noted.

One striking feature of these curves is revealed if the lift increments for the various values of ξ are compared directly, as in Figs. 21a and b. The contribution due to the body grows rapidly with ξ, as would be expected, but that from the wing does not change significantly as ξ increases from 4° to 6·7°. The higher pressures from the larger body act on a smaller exposed wing area, giving a similar wing-lift increment in both cases. For the family of models then, the total lift increment is dominated by the body contribution for the larger bodies, and this may be illustrated (as in Fig. 23a) by considering how the relative contributions to the overall lift vary with ξ at a given incidence. For the case chosen ($\alpha = 4°$) the body contribution to the total is larger when $\xi > 4°$.

12

The results for the $\varepsilon = 15°$ models are very similar to those just discussed and need not be commented upon in detail. Some small differences do occur in the shapes of some of the curves for the two families. For example, the total induced-lift curve for the 15°/10° combination reaches a maximum near 5° incidence (Fig. 20b) whereas that for the 10°/6·7° model, which has the same ratio (ε/ξ), increases after a minimum near 2° incidence. Both the wing and body curves are slightly different in shape, for reasons which are at present unknown, but which may be simply a result of the strange shape of the wing curves in Fig. 11b at low incidence and the inherent inaccuracies. It is felt that too much attention should not be paid to differences of this sort.* This essential similarity between the two sets of results is apparent if Figs. 23a and b are compared. The lack of scatter in these two Figures, incidentally, gives some confidence to the actual values of ΔC_L found from integrating the rather unsatisfactory induced-loading curves.

The information contained in Fig. 23 may be presented in a slightly different form, as in Fig. 24 where the actual (and not the percentage) induced-lift coefficients are compared for an incidence of 4°. The wing contributions each reach a maximum when the cone half-angle is about 2/3 of the wing half-angle. The body lift increment (ΔL), at a given value of ξ, is similar on either wing, but when reduced to coefficient form the larger wing area of the $\varepsilon = 15°$ models causes the body ΔC_L to be about 2/3 of those for the 10° models. At the higher values of ξ, this reduction in body ΔC_L on the larger models is balanced to some extent by a bigger wing contribution and the total induced-lift contribution (Fig. 24) is similar for both sets of model. Diagrams of the type shown in Fig. 24 may be used to estimate the ΔC_L due to the exposed wing area on the 15°/13° combination, a quantity which cannot be found directly.

Figs. 13a and b suggest that cone-flow theory and, for $\xi = 4°$, slender-body theory, may be used to predict the induced-pressure increment on the wing lower surface. The actual lift coefficient change (ΔC_L) may of course be found by integrating these theoretical pressures over the exposed wing surface.

Using slender-body theory this lift-coefficient increment at $\alpha = 0°$ for the $\varepsilon = 15°$ combination is

$$\Delta C_L = 2S \tan^2 \xi, \tag{3}$$

where
$$S = \cos^{-1}(B \tan \xi) - B \tan \xi \cosh^{-1}\left(\frac{\cot \xi}{B}\right).$$

For $M_0 = 4·03$, $\xi = 4°$, this gives a value of ΔC_L of $0·0074_4$, compared with the experimental value of $0·007$ at $\alpha = 0·8°$. This difference is negligible in view of the errors which can arise in deducing ΔC_L from the experimental data. The theory, which assumes a sonic leading edge is not really appropriate for $\varepsilon = 10°$, $\xi = 4°$, but Fig. 13a shows that it must give a close approximation in this case also.

The cone-flow theory is equally good at $\xi = 4°$, and markedly superior for the other two bodies used with the 15° wing. The value of ΔC_L must now be obtained from an integration of the spanwise pressure increment and cannot be expressed in a simple closed form. Since the theoretical trends in the spanwise direction were used to draw the experimental induced loading curves, there is little virtue in comparing theoretical and experimental values of ΔC_L for, say, the 15°/10° model. At present the most that can be said is that cone-flow theory seems to provide a useful guide to the induced lift coefficient at small incidence, and that the simpler slender-body theory may be used if the body angle is small.

We have so far been concerned with the lift increment arising from the lower-surface pressure changes due to the underslung body. As was discussed in Section 3.1.4, the body may influence the upper-surface flow and certainly causes an overall reduction in pressure on this surface in the case of the 10°/10° combination (Fig. 15c). The very scanty evidence for the 10°/6·7° model indicated that the upper-surface effect might then be small as far as pressure changes were concerned. Because complete data are not available and because the prime purpose of the present investigation was to study lower-surface changes, the

---

*For this reason the apparent reduction in wing and body increments between incidences of 7·1° and 8·2° in Fig. 20a is ignored.

body-induced lift increment* on the upper surface has been ignored, the assumption being made that the total lift coefficient on a combination $(C_{L_{WB}})$ is the sum of the lift coefficient on the basic wing (C_{L_W}) plus the total induced lift coefficient contribution on the lower surface (ΔC_L) when the body is present. Once again it is reasonable to consider the flow only at one chordwise station; Fig. 25 shows that the difference between the four positions is small and may be neglected.

Curves of $C_{L_{WB}}$ are presented in Figs. 26a and b for the two families of models. The full curve presented for the 15°/13° combination excludes the contribution from the small exposed wing area and the effect of adding an estimated increment from Fig. 24a is shown as a broken line. Because this estimate is necessarily rather uncertain at some incidences, it has not been used in the subsequent analysis and the actual values of $C_{L_{WB}}$ for this model are perhaps about 5 per cent low. This will not affect the general conclusion which may be drawn from the tests.

The immediate effect apparent in Figs. 26a and b is that the addition of the body simply reduces the no-lift angle without altering appreciably the lift-curve slope. This follows from the relatively small influence of incidence on ΔC_L. The values of the no-lift incidence (α_0) for all eight models are plotted in Fig. 27. The values of ξ which would give zero lift at zero incidence are about 5·7§ and 7·8§ for the two wings. It is interesting to note that the value of ξ (ξ') for which the wing and body cross-sectional areas are equal (thus giving a symmetrical distribution of volume about the wing undersurface plane) are 5·7° and 7·0° respectively, values which are in fair agreement with those just quoted. Because the lift curves for $\varepsilon = 15°$ are reasonably straight near zero lift, and because the isolated wing lift-curve slope agrees with linear theory (Fig. 18b), the values of α_0 may be readily predicted provided this quantity is known for the wing alone. Even if this were not known experimentally, a value of 2·5°, which gives equal slopes on the upper and lower surfaces, would be a reasonable approximation.

The surface pressure distributions may also be used to find the force acting on the forward-facing surfaces of the body parallel to the wing undersurface. This axial force will have two components, that from the cone surface and that associated with the wing upper surface. The lower wing surface is, by definition, a plane in the axial direction and hence contributes nothing to the axial-pressure force. Both components of the axial pressure forces were found by mechanical integration, added together and then combined with the normal force, obtained earlier, to give finally the pressure-drag coefficient, C_{D_P}. It must be stressed that no allowance has been made for the base drag acting on all eight models, or the changes in upper-surface with cone size; the upper-surface pressure drag is assumed to be independent of the underbody shape.

The pressure-drag curves for the models having a 10° wing are plotted in Fig. 28a, and those obtained with a 15° wing in Fig. 28b. These Figures show that very large pressure drags occur with the larger cones, and hence that the increased lift apparent in Figs. 26a and b for these models incurs a serious drag penalty. The ratio of model lift to pressure drag is plotted in Figs. 29 and 30 against both incidence and lift, and it is apparent that the highest values of this ratio are obtained for the isolated wing. By adding progressively larger bodies a marked reduction in lift/drag ratio takes place. The curves for $\xi = 0°$ have pronounced peaks however, whilst those for the wing-body combination become more and more insensitive to incidence. Moreover, the lift coefficient at which the maximum lift/drag ratio occurs increases considerably with ξ (Figs. 29b, 30b).

These results of course take no account of the drag contribution due to the surface friction. To illustrate the effect that this can have on the lift/drag curves, an estimate has been made of the surface friction at the test Reynolds number for all eight configurations. For each model a wholly laminar or wholly turbulent boundary layer has been assumed, and for simplicity these values have been taken as invariant with incidence. The actual values of the surface-friction coefficient (C_D) were found by considering chordwise strips of the wing and integrating the local friction force across the span. A simple allowance was made for the change in surface friction along the cone surfaces[9]. The modified lift/drag curves are presented in Figs. 31 and 32, where the friction-drag coefficients used are quoted. A more revealing plot is perhaps

---

*This increment is certainly positive for the 10°/10° model, and appears to be so for the 10°/6·7° combination. No information is available for those models with $\varepsilon = 15°$.

that contained in Figs. 33 and 34, where the influence of boundary-layer state on the maximum lift coefficient at which this is achieved is illustrated. It is then apparent that the surface friction has the strongest influence when ξ is small, but that with the larger bodies the pressure drag predominates. It is still true, however, that for either boundary-layer state the small bodies remain aerodynamically most efficient, but over a limited range of lift, whilst the bigger bodies have a performance which is affected little by changes in model attitude. For these large bodies the rather shallow maximum value of lift/drag ratio tends to occur at about the same lift coefficient.

In other investigations both theoretical estimates and experimental results have been obtained for lift/drag ratios of delta wing and half-cone combinations. Migotsky and Adams[11], for example, use slender-body theory applied to a sonic-edged wing and its underslung body. The broken curve in Fig. 34a has been taken from their results, and though the curve is roughly similar in shape to the ones derived from the present tests, it tends to give too large a lift/drag ratio, particularly for the bigger bodies where, as was shown earlier, slender-body theory is not really appropriate.

Most experimental determinations of lift/drag ratios have employed strain-gauge balances (e.g. Refs. 12 and 13) and in consequence the drag of the base area is included in the total drag of the model. Comparison with the present results is therefore of rather limited value. However, a comparison is made in Fig. 32b with balance results from Model 1 of Ref. 12 for which $\varepsilon = 12 \cdot 4°$, $\xi = 5°$, $M_0 = 4 \cdot 24$ and the test Reynolds number is 4·7 million. The boundary-layer state is unknown and in order to use Fig. 32, the incidence for the results contained in Ref. 12 has been adjusted so that this combination has the same no-lift angle as the present 15°/4° combination. As can be seen the general shape of the balance-test curve is similar to those obtained by integrating the surface pressure distributions and then adding an estimate of the surface-friction drag.

It is sometimes suggested (Ref. 14, for example) that a useful correlating parameter for the maximum lift/drag ratio of a family of hypersonic vehicles of the present type is $V_B^{2/3}/A_W$, where V_B is the body volume and A_W is the wing plan area. This parameter is used in Fig. 35 for the results with either completely laminar or turbulent boundary layers, but only fair correlation is achieved. The general trend and level is, however, similar to that found by McLellan and Ladson in Ref. 14. Because in the present tests the wing volume is comparatively large it may be argued that the volume used in the parameter should be that of the whole configuration and not that of the underslung body alone. This change does does not give any noticeable improvement in the correlation.

4. Concluding Remarks.

As was mentioned in the Introduction, the present investigation is a preliminary one, aimed at obtaining a limited understanding of the flow problems involved, together with a fuller appreciation of the form of the problems themselves. As far as possible, most stress has been laid upon the way the flow fields associated with the wing and body interact, since it is felt that in this way can useful progress be made most readily. It would seem that for the flow close to the junction of the wing and body the resultant pressure is near that obtained by adding the local increment due to the wing to the local pressure on an isolated cone. This superposition effect becomes less and less valid as the most windward generator of the cone is approached; at this position the wing has no influence, the pressures being close to that for an isolated cone. As would be expected, when the body occupies the entire lower surface, the pressures on the half cone are similar to those on the forward surface of a complete isolated cone of similar angle. The addition of even a small region of exposed wing area, however, greatly modifies the pressure over a large part of the cone surface, an effect which increases the undersurface lift.

On the exposed wing undersurface at small incidences the pressure increment associated with the half cone seems to be well predicted from a knowledge of the isolated cone flow field. For cones of small semi-vertex angle, slender-body theory can be used instead, but in general its validity at high supersonic speeds is questionable. One the pressure-increment distribution is known, the lower-surface lift increment can easily be found. The effect of applying incidence to the combination is generally to reduce the induced pressures on the wing, mainly because these are linked to the pressures on the cone near the junction, which fall as incidence is applied. For the smallest cone tested this trend was reversed to a slight degree

15

and this may be due to the boundary-layer growth in the junction. Apart from this aspect, the boundary-layer in this region does not appear to influence the local flow to any great extent, contrary to expectations.

Because the induced pressures on the wing are generally lower at incidence, the body-induced lift on the wing lower surface decreases with rising incidence, unlike the body lift increment, which is dominated by the rapidly-increasing pressure near the most windward generator. The total lower-surface lift increment tends to rise slowly with incidence, but when the total lift of the combination is considered this incidence variation is swamped by that associated with the wing. To good approximation the effect of adding the body is to alter the no-lift angle of the model but not to change the lift-curve slope.

There is some evidence in the present tests that for large bodies the upper-surface flow is altered by the underbody, with a resultant small increase in lift. This effect seems to come mainly, but not entirely, from an alteration in the way the separated flow develops with incidence on the upper surface.

Though the half-cone bodies produce an appreciable change in lift at a given incidence, this is accompanied by a considerable increase in drag. As a result the highest values of the lift/drag ratio occur for the isolated wings and the lowest for those models with the largest bodies. The latter models, however, retain a lift/drag ratio close to their maximum for a wide range of incidence, a useful feature for re-entry manoeuvres, whereas the isolated wings or those combinations with small bodies have pronounced peaks in the lift/drag curves. For continuous cruise conditions this class of configurations would be aerodynamically more efficient.

The present tests reveal little change in behaviour which can be attributed directly to the presence of a subsonic leading edge on the 10° wing and a near-sonic edge on the 15° wing. Further work with a less highly-swept (and therefore strongly supersonic) leading edge would be valuable in allowing some assessment to be made as to whether the cone flow field is effectively limited by a simple near-conical shock wave, with the region near the wing tips dominated by two-dimensional flow over the inclined wing surface (Fig. 36a),* or whether a single curved shock occurs, as on Fig. 36b. Some experimental evidence (Ref. 14, for example) suggests that for highly-swept wings a single shock occurs, and that the body influence spreads to the wing tip. On the other hand, the vapour-screen photographs in Ref. 8 show a shock pattern similar to that sketched in Fig. 36a. If the cone shock wave does penetrate to the under-wing surface, shock-wave and boundary-layer interaction phenomena should occur with important influences on the model characteristics.

Allied to these problems of the flow pattern for well-supersonic leading edges is that of the shock system changes which occur when the model is at yaw. So far only limited tests have been reported[8] and much more work is required. Similarly the influence of marked wing anhedral and dihedral may become important in improving the vehicle performance. This topic has received some attention in the U.S.A. where force tests have been made on a variety of bodies, including those with drooped tips. These tests suggest that in general an asymmetric wing together with a body has a maximum lift/drag ratio not greatly different from a more conventional wing and body configuration[14]. This result is at first sight somewhat surprising and will only be explained satisfactorily when the detailed flow field is known in both cases. It may well be that at high supersonic speeds changes in surface geometry, for a given volume, cause changes in the enveloping shock-wave system in such a way that the net normal and axial pressure forces are relatively unchanged. This again emphasises the urgent need for a basic understanding of the relationship between shock and body shape on lifting vehicles. Without this, it seems likely that progress will be piecemeal and slow.

5. Acknowledgements.

---

*These Figures are meant to be diagrammatic only and are not intended to depict accurately the flow and shock pattern close to the junction.

16

REFERENCES

No.	Author(s)	Title, etc.

1   L. C. Squire   ..   ..   ..

Pressure distributions and flow patterns at $M = 4.0$ on some delta wings
     Part I   Wings of inverted 'V' cross-section.
     Part II   Flat wings.
A.R.C. R. & M. 3373, February, 1963.

2   J. L. Amick   ..   ..   ..

Pressure measurements on sharp and blunt 5°-and 15°-half-angle cones at Mach number 3·86 and angles of attack to 100°.
NASA TN D-753, February, 1961.

5   D. H. Peckham ..   ..   ..

Experiments at hypersonic speeds on circular cones at incidence.
A.R.C. C.P.702
January, 1963.

4   M. Holt and J. Blackie ..   ..

Experiments on circular cones at yaw in supersonic flow.
J. Aeronaut Sci., 23, pp.931–6, 1956.

5   Z. Kopal..   ..   ..   ..

Tables of supersonic flow around cones.
Tech. Report No. 1: M.I.T., 1947.

6   J. D. Julius   ..   ..   ..

Measurements of pressure and local heat transfer on a 20° cone at angles of attack up to 20° for a Mach number of 4·95.
NASA TN D–179, December, 1959.

7   R. C. Savin   ..   ..   ..

Approximate solutions for the flow about flat-top wing-body configurations at high supersonic airspeeds.
NACA RM A58F02 (TIL 6153), September, 1958.

8   R. E. Randall, D. R. Bell and J. L. Burk

Pressure distribution tests of several sharp leading-edge wings, bodies and body-wing combinations at Mach 5 and 8.
AEDC–TN–60–173, September, 1960.

9   A. H. Shapiro   ..   ..   ..

The Dynamics and Thermodynamics of Compressible Fluid Flow. Vol. II, Chapters 26 and 27.
The Ronald Press Co., New York, 1954.

10   L. Rosenhead et al   ..   ..

A selection of graphs for use in calculations of compressible airflow.
Oxford University Press, 1954.

11   E. Migotsky and G. J. Adams ..

Some properties of wing and half-body arrangements at supersonic speeds.
NACA RM A57E15 (TIL 5603), July, 1957.

12   C. A. Syvertson, T. J. Wong and H. R. Gloria

Additional experiments with flat-top wing-body combinations at high supersonic speeds.
NACA RM A56I11 (TIL 5430), February, 1957.

13   W. O. Armstrong and ..   .. C. L. Ladson

Unpublished NASA Report.

14   C. H. McLellan and   ..   .. C. L. Ladson

Unpublished NASA report.

17

REFERENCES—*continued*

No.	*Author(s)*	*Title, etc.*
15	J. W. Reyn and J. H. Clarke ..	An assessment of body lift contributions and of linearized theory for some particular wing-body combinations. Polytechnic Inst., Brooklyn. PIBAL Report 305, June, 1956.
16	E. W. E. Rogers and C. J. Berry	Experiments at $M = 1\cdot41$ on elliptic cones with subsonic leading edges. A.R.C. R. & M. 3042, October, 1955.

Wing pressure holes occur at same
positions on both surfaces except
for row $\theta = 0^0$, which is only on
lower surface

x / c

0·4 →

0·6 →

0·8 →

0·95 →

$\epsilon = 10^0$

.5″

$\theta = 7^0$ 0^0 5^0 8.5^0

0·4375″ at base

No body

$\xi = 4 \cdot 0^0$

$\xi = 6 \cdot 7^0$

Body pressure holes are at
same values of ϕ for all
three bodies, and occur at
$x/c = 0.4, 0.6, 0.8$ and 0.95

$\phi = 45^0$

15^0

60^0

90^0

$\xi = 10 \cdot 0^0$
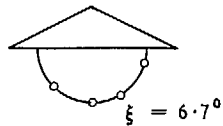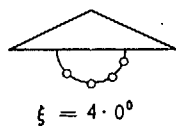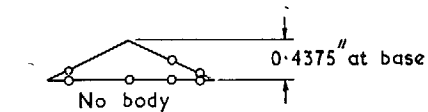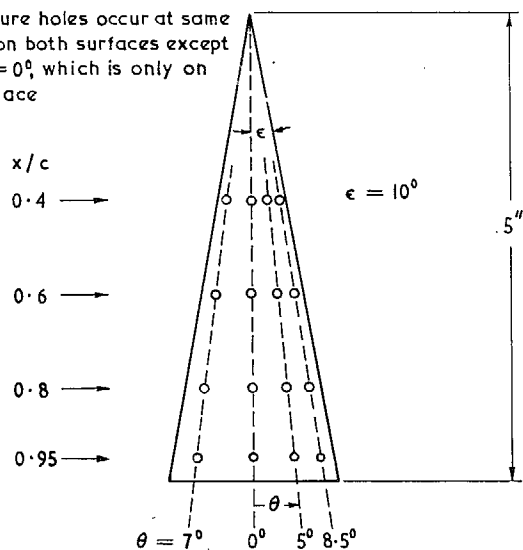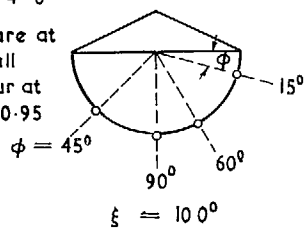
FIG. 1a.   Details of models with $\varepsilon = 10°$
(80° sweepback).

Wing pressure holes occur at same
positions on both surfaces, except
for row $\theta = 0^0$, which is only on
lower surface

x / c

0·4 →

0·6 →

0·8 →

0·95 →

$\epsilon = 15^0$

5″

$\theta = 12^0\ 8\cdot5^0$ 0^0 $6^0\ 11\cdot5^0$

0·4375″ at base

No body

$\xi = 4 \cdot 0^0$

$\xi = 10 \cdot 0^0$

Body pressure holes are
at same values of ϕ for all
three bodies and occur at
$x/c = 0.4, 0.6, 0.8$ and 0.95

$\phi = 45^0$

15^0

60^0

80^0

$\xi = 13 \cdot 0^0$
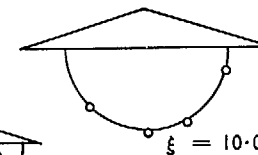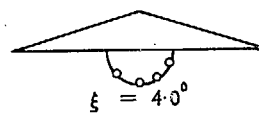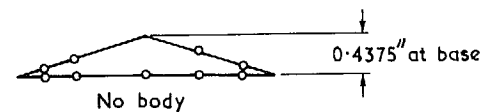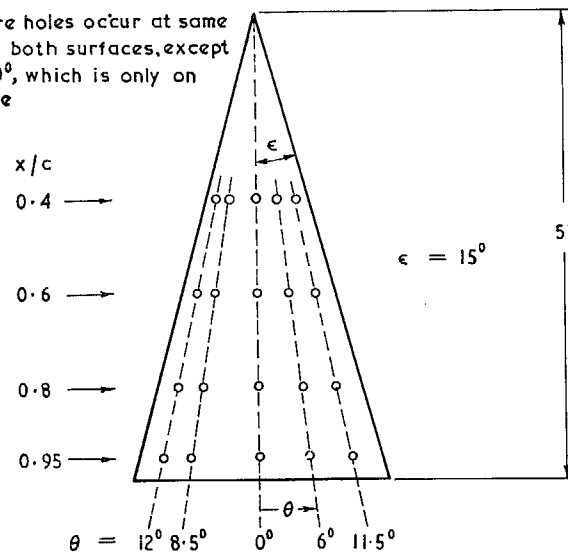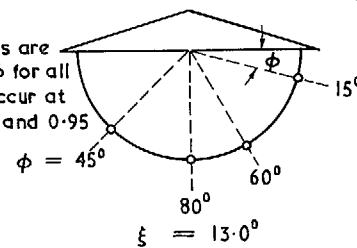
FIG. 1b.   Details of models with $\varepsilon = 15°$
(75° sweepback).

FIG. 1c.   Side elevations of wing—
body models.
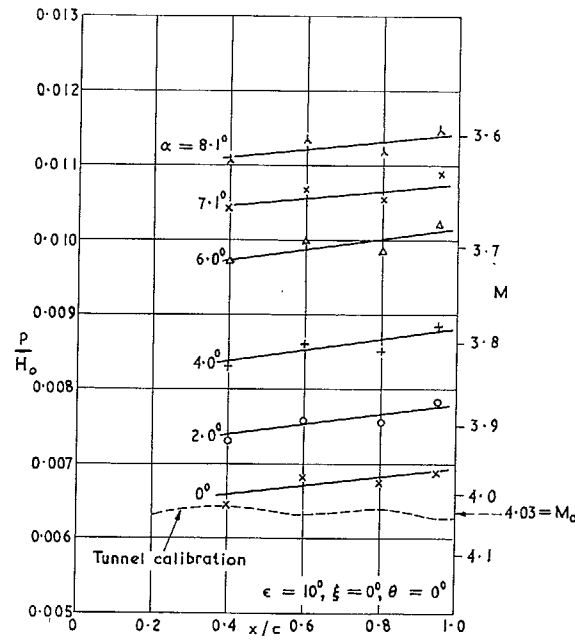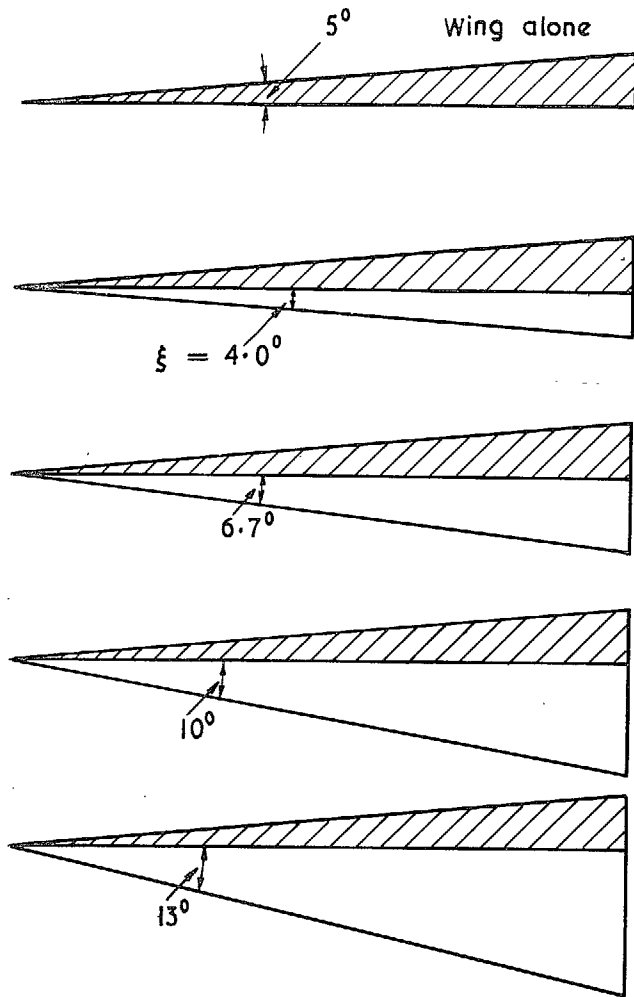
FIG. 2a.   Pressure   distributions
on   10° wing undersurface on
centreline; no body.
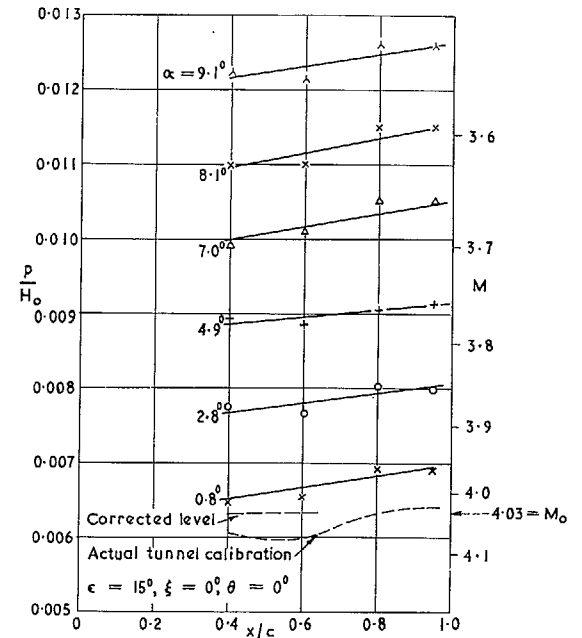
FIG. 2b.   Pressure   distributions
on   15° °wing undersurface   at
centreline; no body.

(N.B. values of $\frac{p}{H_0}$ at $\frac{x}{c} = 0.4$ and
0.6 have been corrected for tunnel
pressure gradient.)
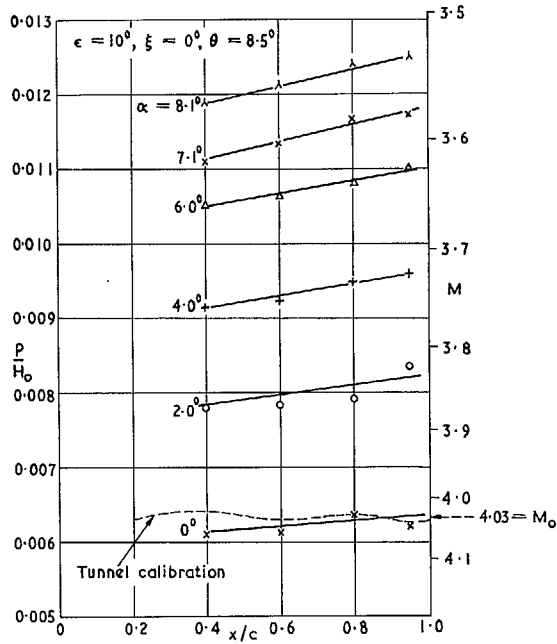
FIG. 3. Pressure distributions on 10° wing undersurface on ray $\theta = 8.5°$; no body.
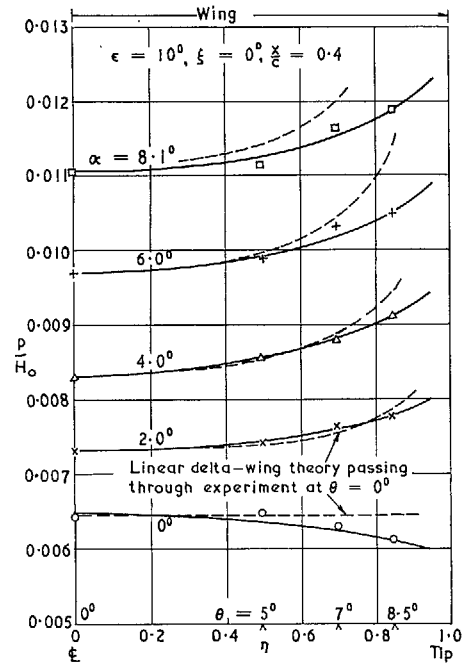
FIG. 4a. Spanwise pressure distribution on 10° wing undersurface; no body.
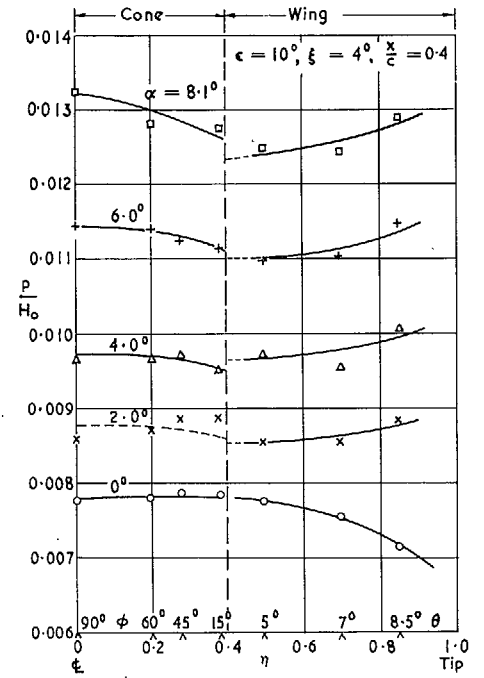
FIG. 4b. Pressure distribution on undersurface of 10°/4° combination.
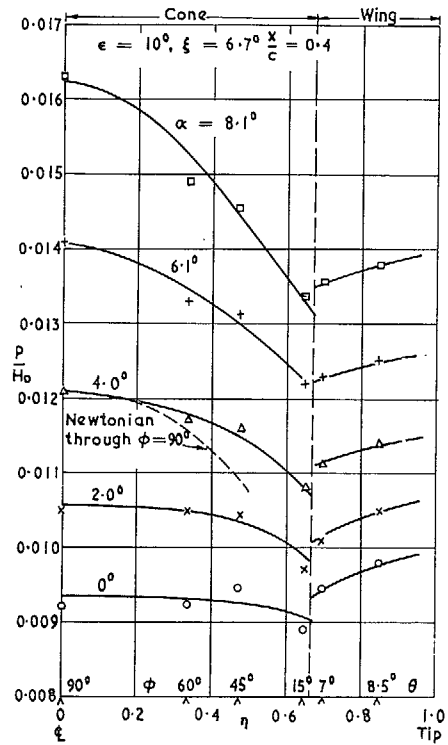
FIG. 4c.   Pressure distribution on undersurface of 10°/6·7° combination.
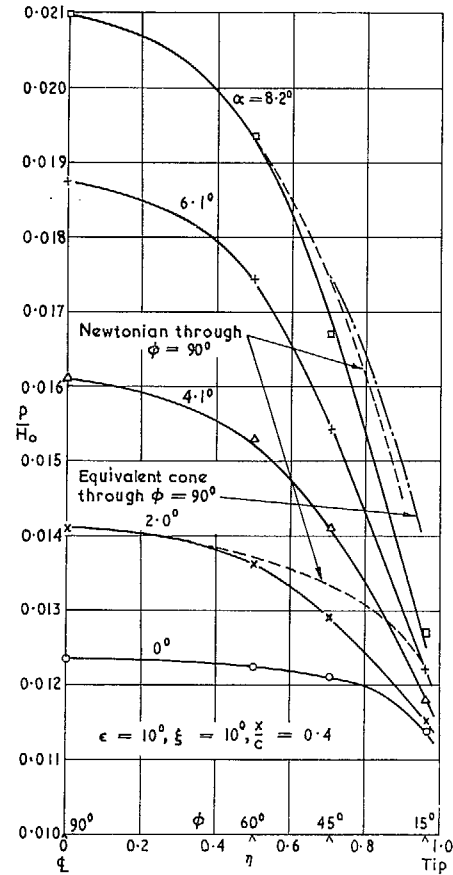
FIG. 4d.   Pressure distribution on undersurface of 10°/10° combination.
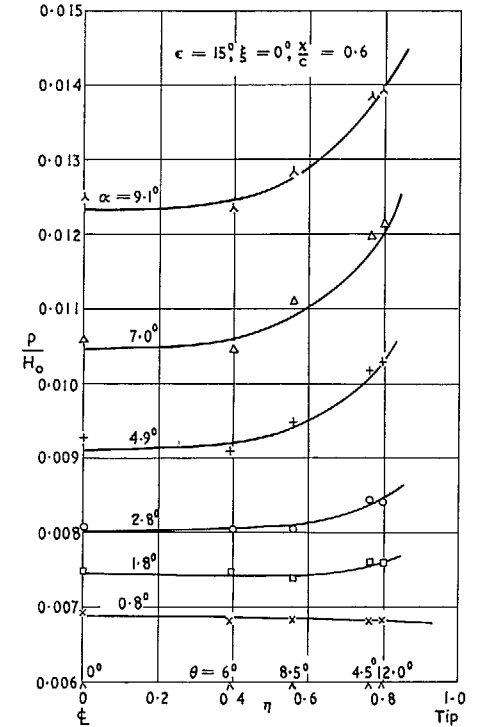
FIG. 5a.   Spanwise pressure distribution on 15° wing undersurface; no body.

22
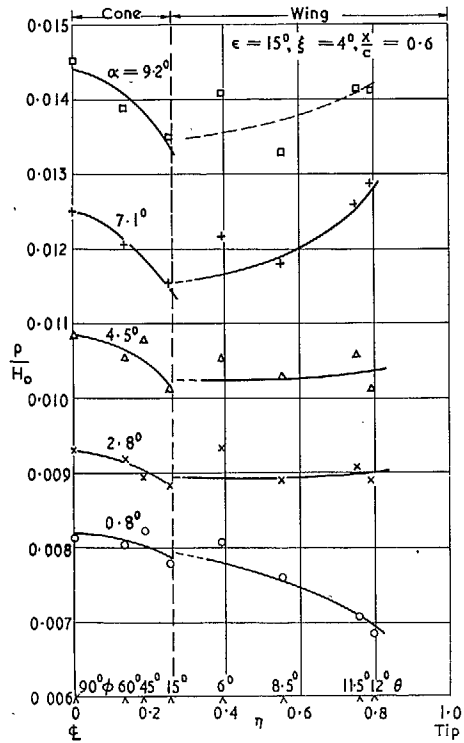
FIG. 5b. Pressure distribution on
on undersurface of 15°/4° com-
bination
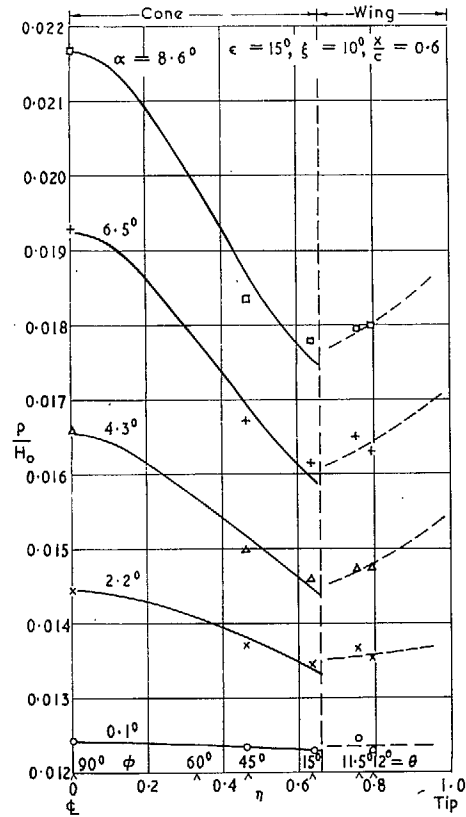
FIG. 5c. Pressure distribution on
undersurface of 15°/10° combina-
tion. (Data not available at
$\phi = 60°$.)

Distribution on exposed wing
surface uncertain.
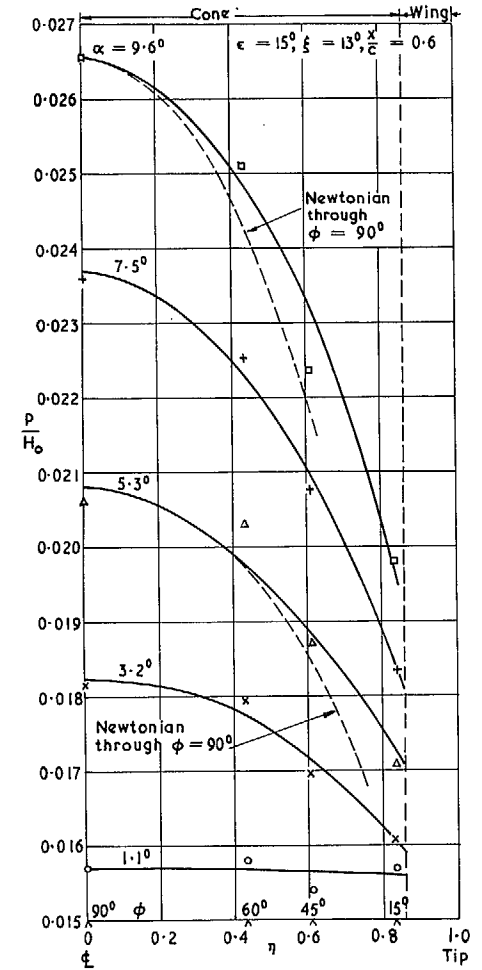
FIG. 5d. Pressure distribution on
undersurface of 15°/13° com-
bination.

FIG. 6a. Graph labels:

Squire (Ref.1): wing with $\epsilon = 18\cdot5^0$, at $M = 3\cdot97$

Exact wedge theory

Experiment $\left(\frac{x}{c} = 0\cdot4\right)$

Equivalent wedge linear theory

Linear theory for delta wing $(M_0 = 4\cdot03, \epsilon = 10^0, \theta = 0^0)$

Newtonian: $C_p = 2\sin^2\alpha$

$\frac{P}{H_0}$
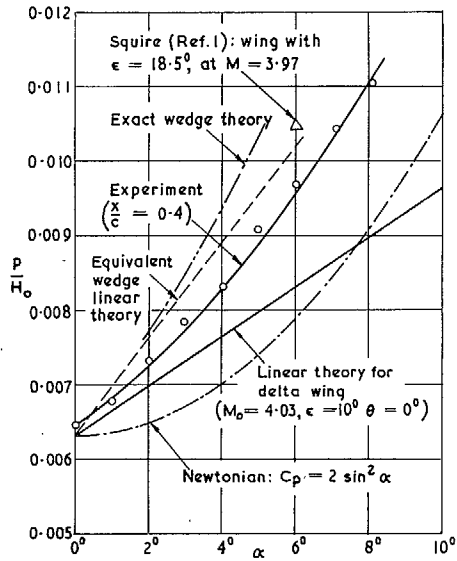
FIG. 6a. Comparison between experiment and linear theory for 10° wing undersurface at $\theta = 0^\circ$.

FIG. 6b. Graph labels:

$\phi = 90^0, \eta = 0^0$

—△— $10^0/4^0$ combination
+ $15^0/4^0$ combination

Newtonian for cone: $C_p = 2\sin^2(\xi+\alpha)$

Tangent–cone approximation $(M_0 = 4\cdot03)$

$\frac{P}{H_0}$

$\eta = 0^0$

—○— 10^0 wing alone
x 15^0 wing alone
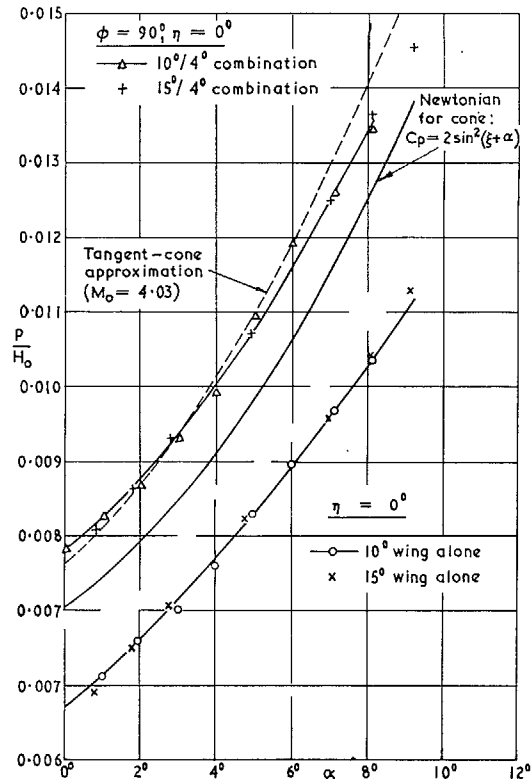
FIG. 6b. Influence of incidence and wing angle on pressures observed on cone at most windward generator ($\phi = 90^\circ$) and on centreline of wing alone ($\eta = 0$);
$$\frac{x}{c} = 0\cdot6.$$

FIG. 6c. Graph labels:

Cone and Newtonian

Tangent–cone approximation $(M_0 = 4\cdot03)$

$\frac{P}{H_0}$

—○— $10^0/10^0$ combination
x $15^0/10^0$ combination
$\frac{x}{c} = 0\cdot6, \phi = 90^0$
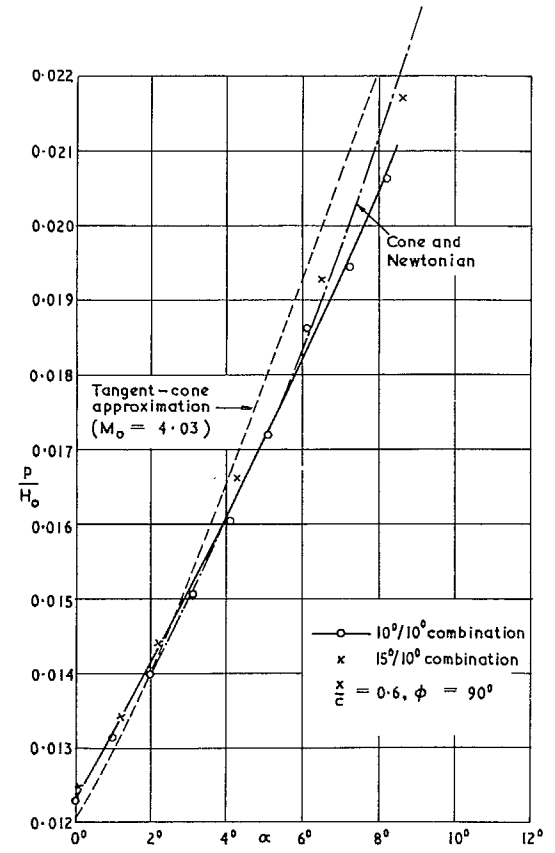
FIG. 6c. Influence of incidence on pressures observed on cone at most windward generator ($\phi = 90^\circ$) for both values of ε and $\xi = 10^\circ$.
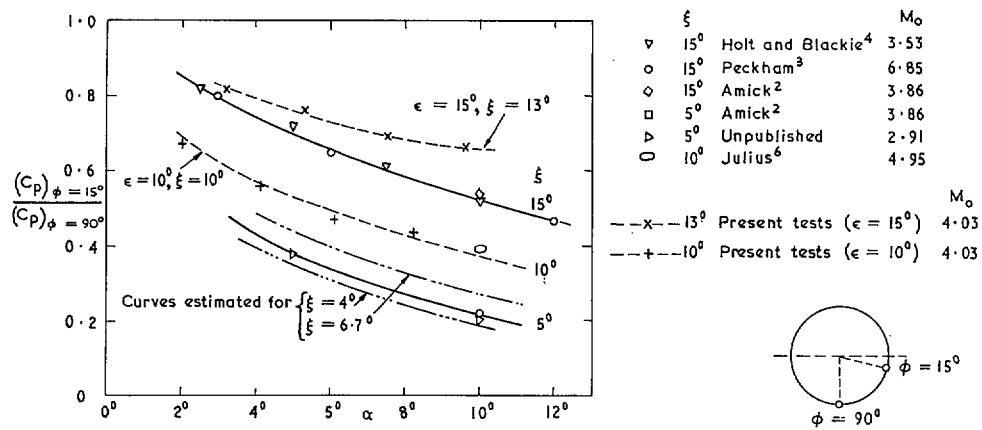
FIG. 7.   Cone-surface pressure ratio, showing influence of wing on 15°/13° combination.
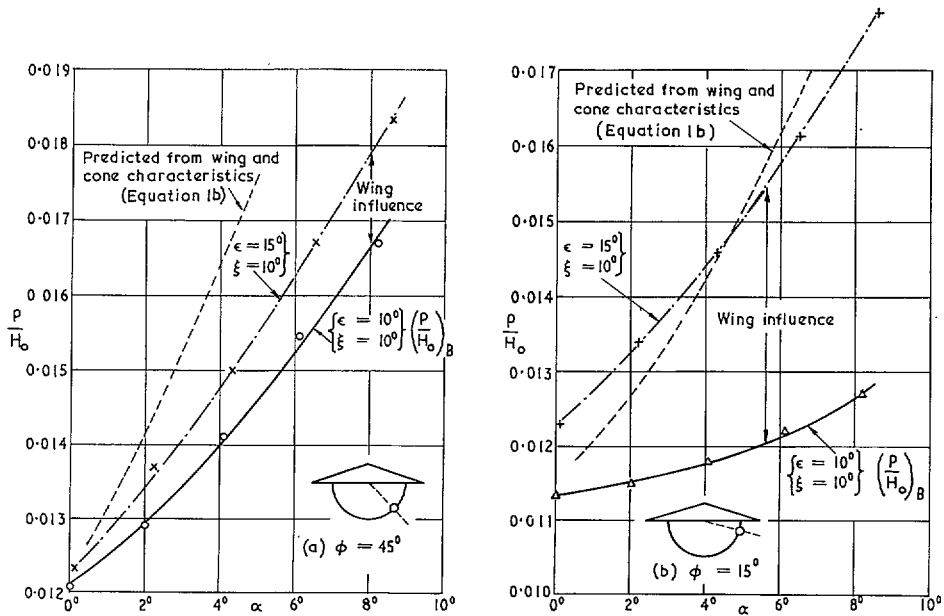
FIG. 8.   Influence of exposed wing surface on adjacent cone-surface pressures $(\frac{x}{c} = 0.4)$.

$$\left(\frac{p}{H_o}\right)_{WB} = \left(\frac{p}{H_o}\right)_B + F\left[\frac{p}{H_o} - \frac{p_o}{H_o}\right]_W$$

○ $\epsilon = 15^\circ,\ \xi = 10^\circ$
× $\epsilon = 10^\circ,\ \xi = 4^\circ$
+ $\epsilon = 15^\circ,\ \xi = 4^\circ$
△ $\epsilon = 10^\circ,\ \xi = 6 \cdot 7^\circ$
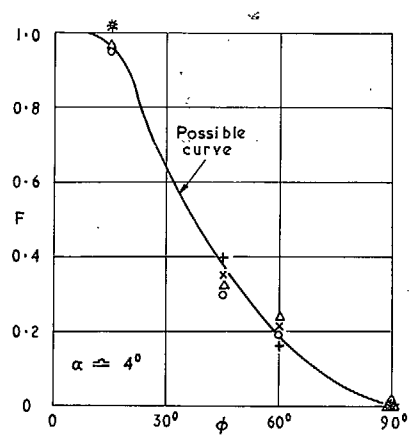
FIG. 9. Suggested influence factor for estimating pressures on half-cone bodies placed under delta wing.
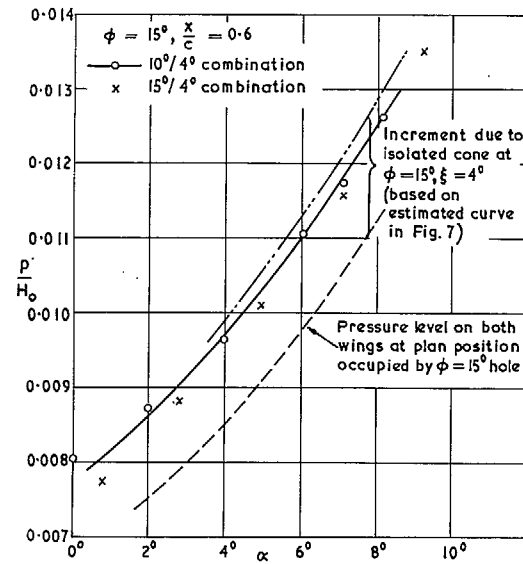
FIG. 10. Comparison of pressures at $\phi = 15^\circ$ on two combinations having $\xi = 4^\circ$, showing independence from wing angle ε.
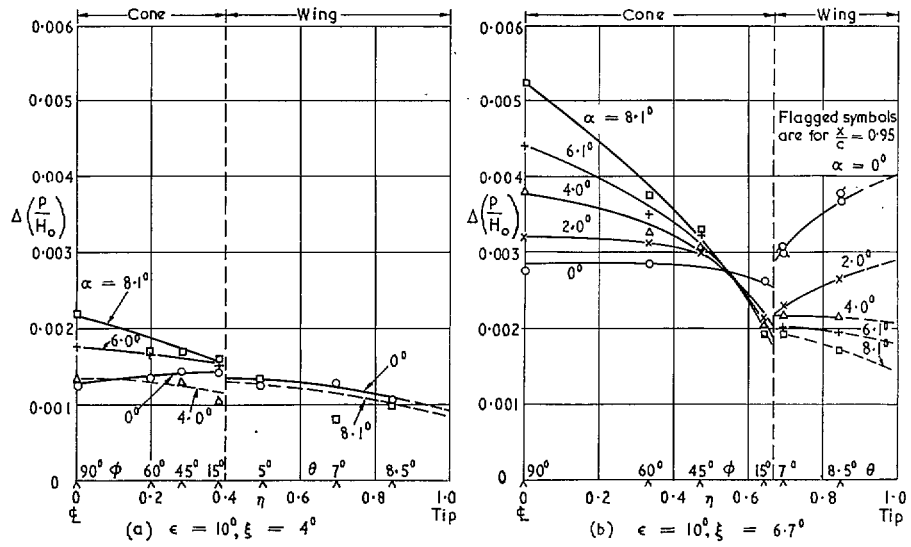
FIG. 11a and b. Body-induced pressure changes on model lower surface ($\frac{x}{c} = 0.4$).
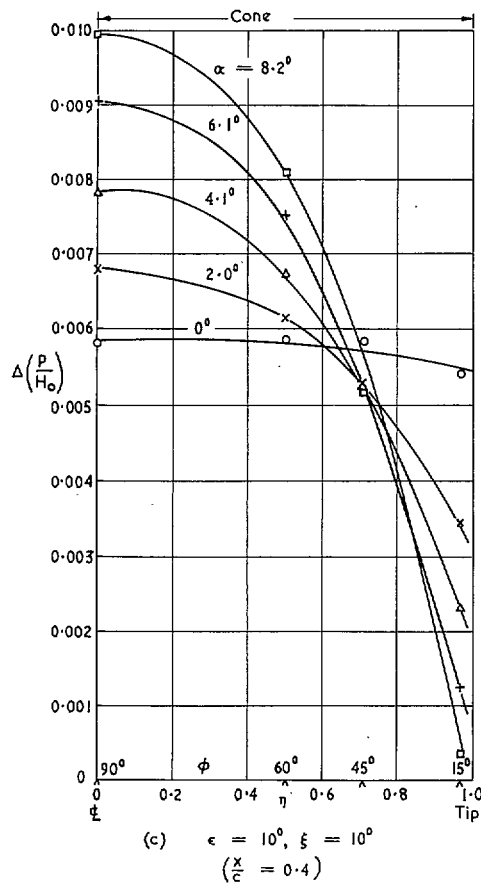
FIG. 11c. Body-induced pressure changes on model lower rurface.

27
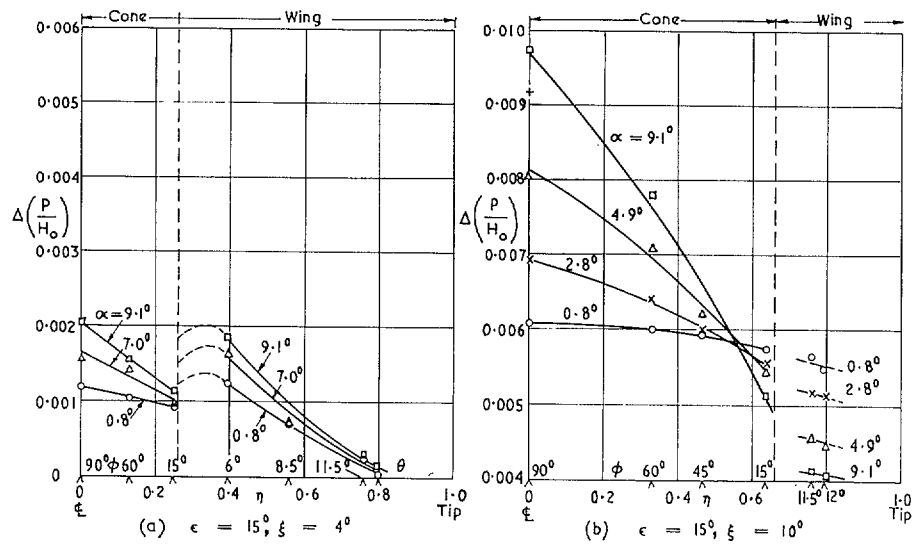
FIG. 12a and b. Body-induced pressure changes on model lower surface ($x/c = 0.6$).
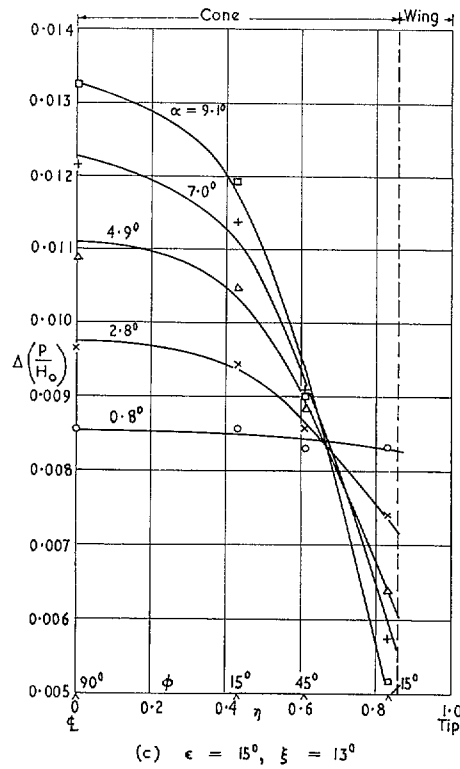
FIG. 12c. Body-induced pressure changes on model lower surface ($\frac{x}{c} = 0.6$).
(No pressure holes on exposed wing area).

28
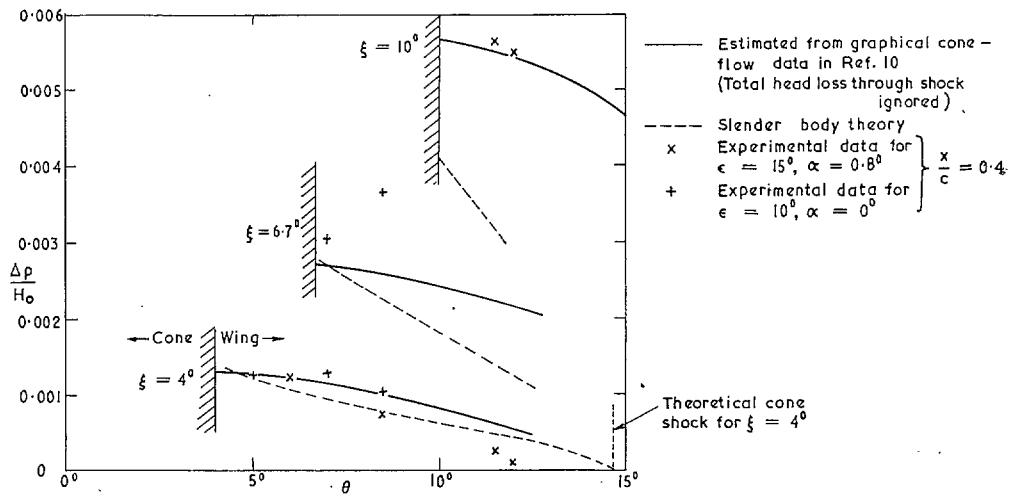
FIG. 13a. Comparison between theoretical and experimental induced loadings at $\alpha \simeq 0°$, $M_0 = 4.03$.
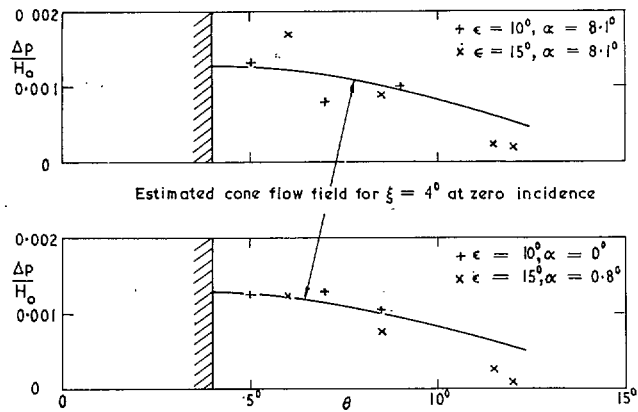
FIG. 13b. Induced field on wing undersurface for smallest half-cone; influence of model incidence.
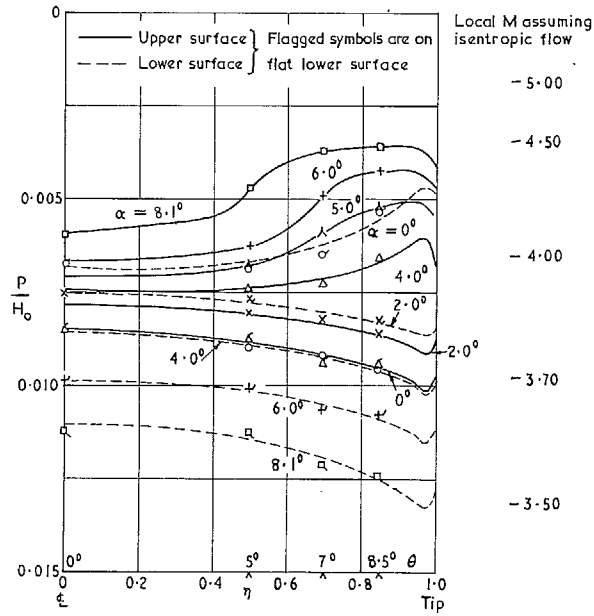
FIG. 14a.   Spanwise pressure distributions for wing
(ε = 10°) alone
(x/c = 0·8).
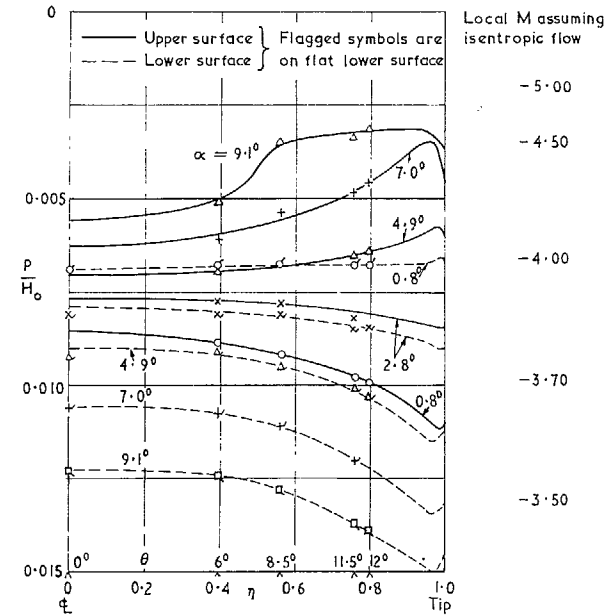
FIG. 14b.   Spanwise pressure distributions for
wing (ε = 15°) alone
(x/c = 0·6).
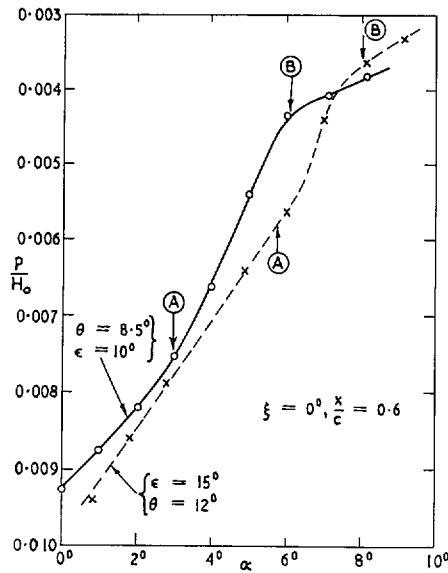
FIG. 15a. Influence of separation growth on surface pressures.
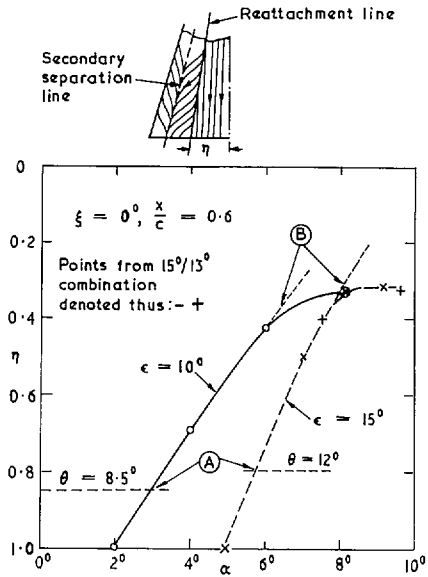
FIG. 15b. Movement of reattachment line with incidence.
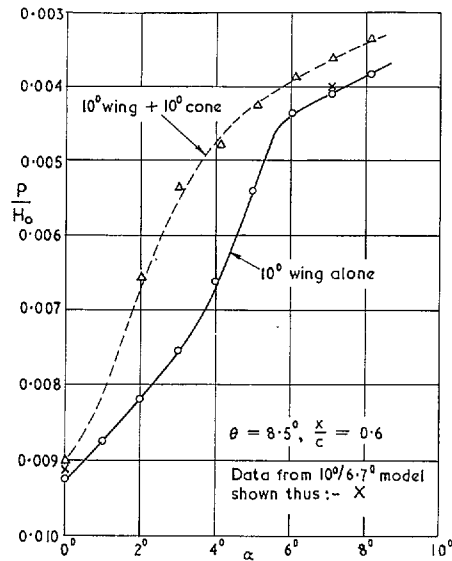
FIG. 15c. Effect of large half-body on upper-surface pressures.

31

$\epsilon = 15^0, \xi = 13^0, \alpha = 7 \cdot 5^0$ (with body)
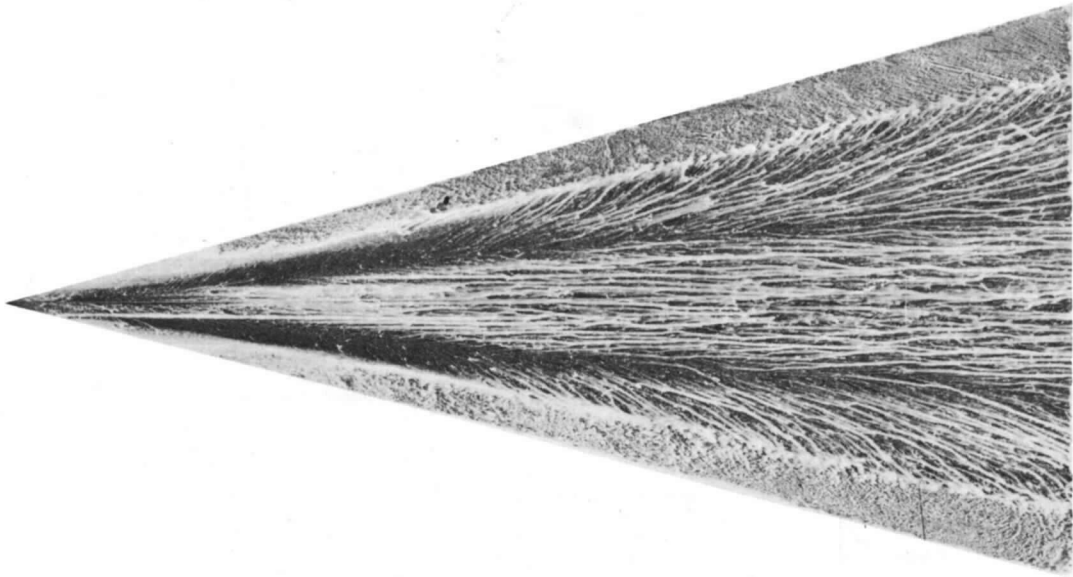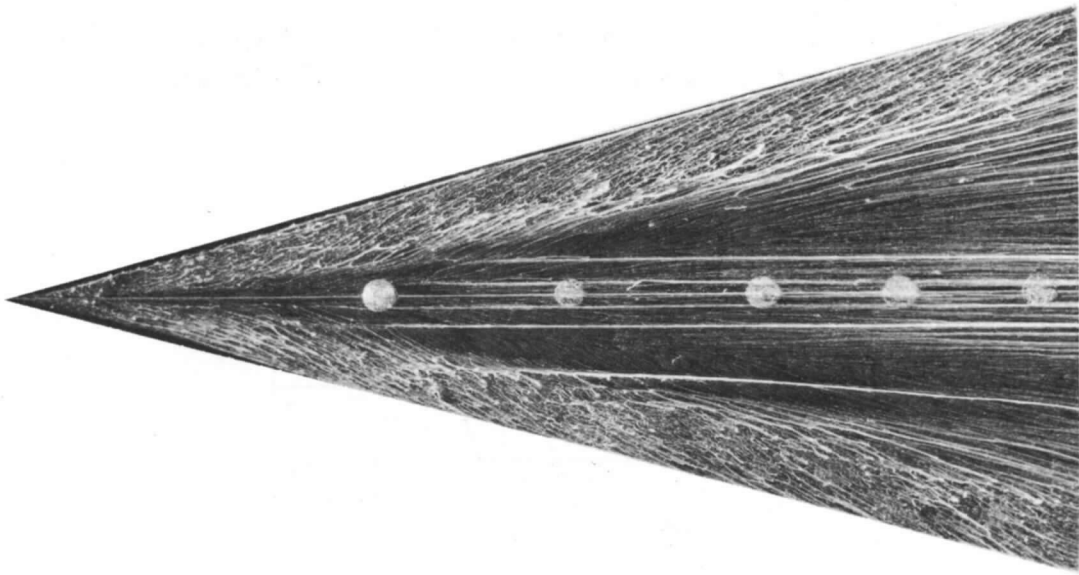
$\epsilon = 15^0, \xi = 0^0, \alpha = 8^0$ (without body)

FIG. 16. Influence of lower-surface body on upper-surface oil patterns.
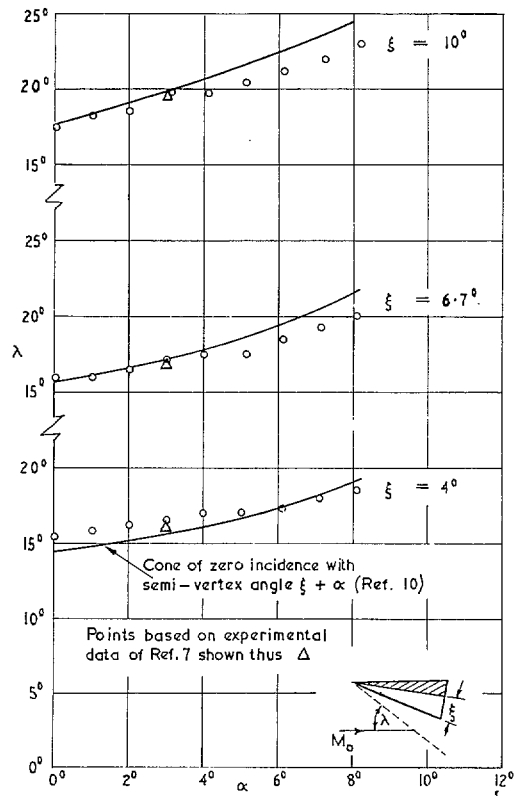
FIG. 17.   Effect of incidence on undersurface shock in plane. $\phi = 90°$.
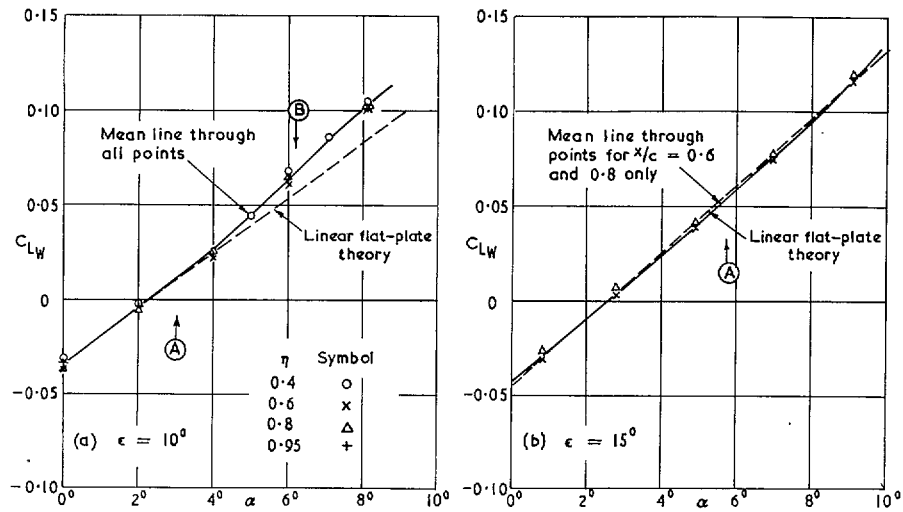
FIG. 18a and b.   Lift curves of two wings ($\varepsilon = 10°, 15°$) alone.

33
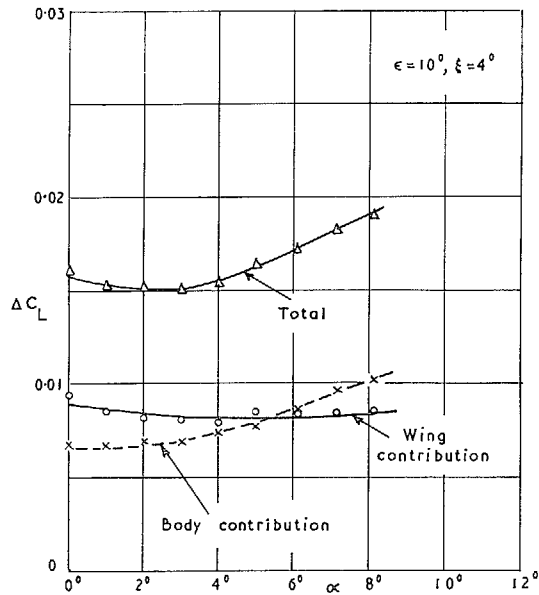
FIG. 19a. Lift-coefficient increment on 10°/4° combination, based on data obtained at $x/c = 0.4$.
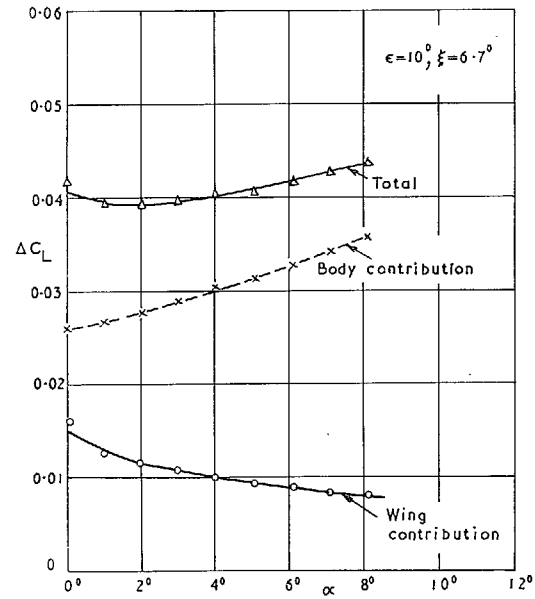
FIG. 19b. Lift-coefficient increment on 10°/6·7° combination, based on data obtained at $x/c = 0.4$.
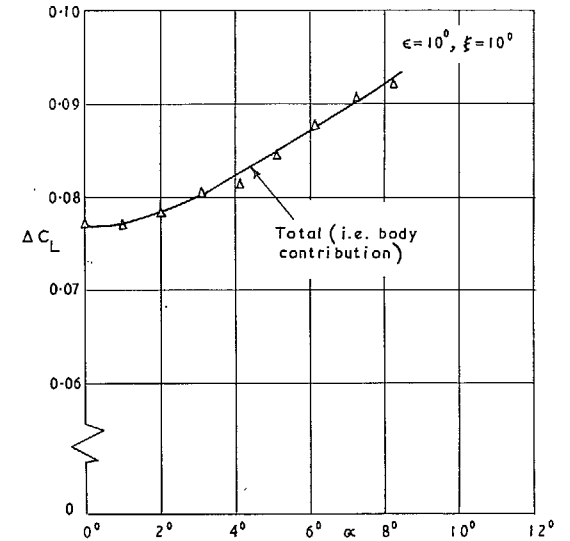
FIG. 19c. Lift-coefficient increment on 10°/10° combination, based on data obtained at $x/c = 0.4$.

34
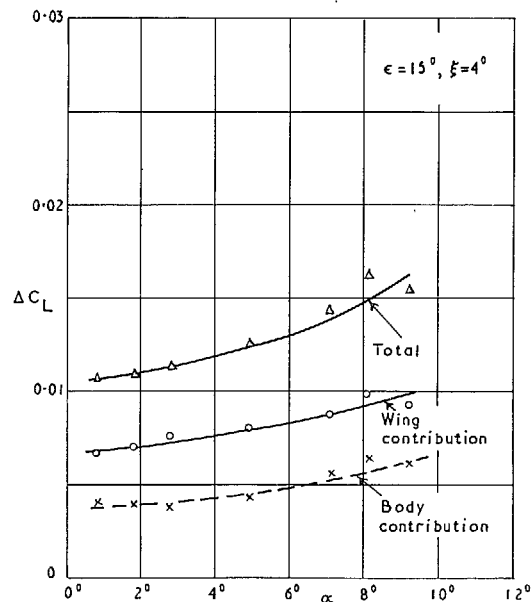
FIG. 20a. Lift-coefficient incre-
ment on 15°/4° combination,
based on data obtained at
$x/c = 0.6$.
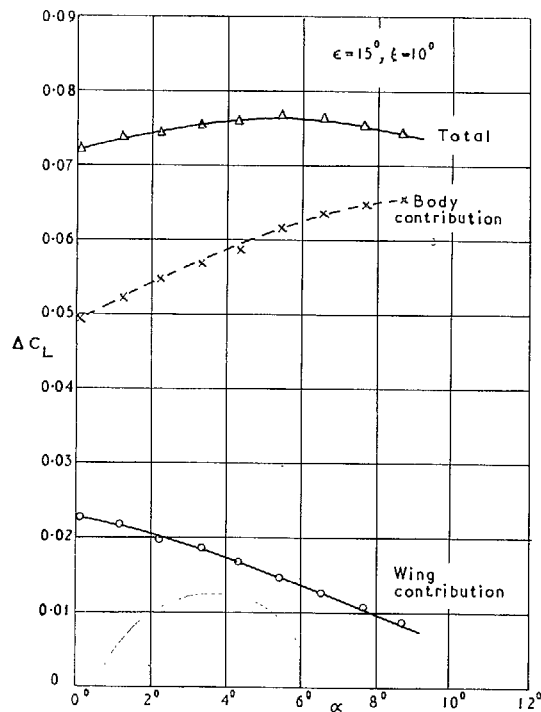
FIG. 20b. Lift-coefficient incre-
ment on 15°/10° combination,
based on data obtained at
$x/c = 0.6$.
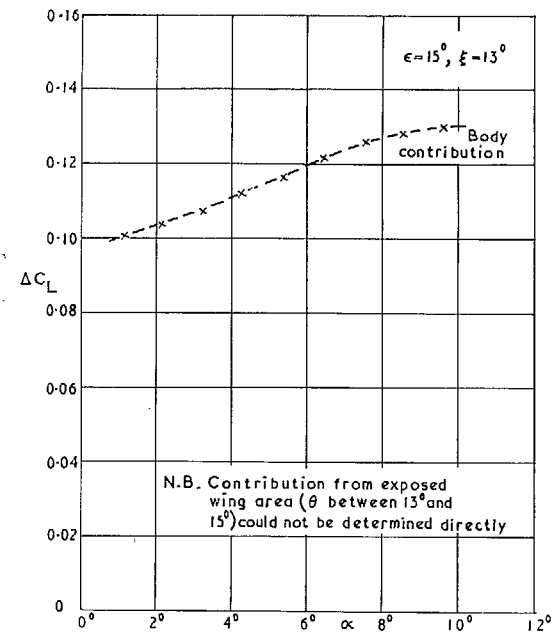
FIG. 20c. Lift-coefficient incre-
ment on 15°/13° combination,
based on data obtained at
$x/c = 0.6$.
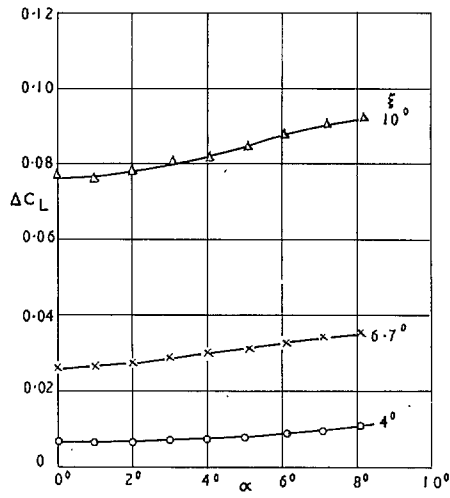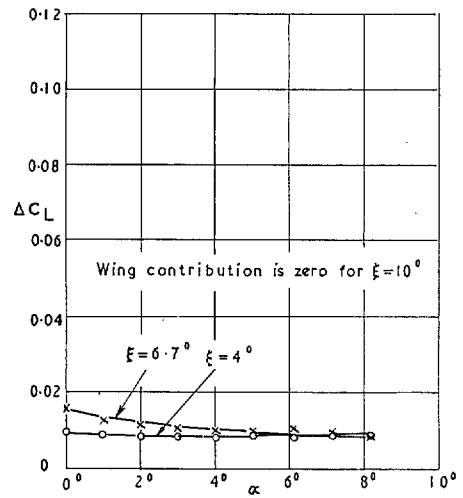
(a) Body contribution (b) Wing contribution

FIG. 21a and b. Variation of lift increments with incidence for wing with $\varepsilon = 10°$.
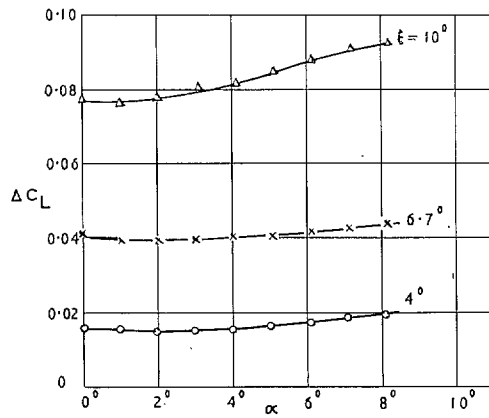
(c) Total contribution

FIG. 21c. Variation of lift increments with incidence for wing with $\varepsilon = 10°$ (contd.).

36
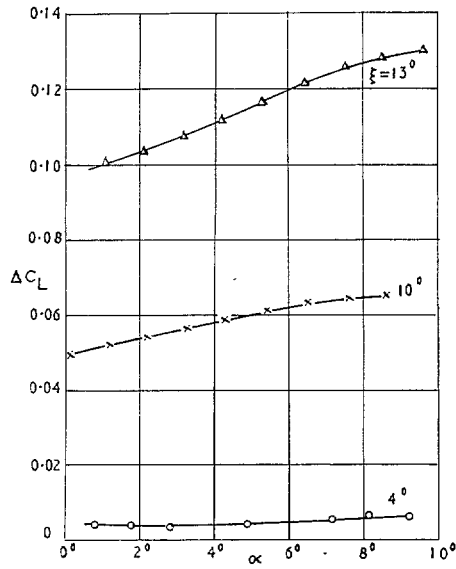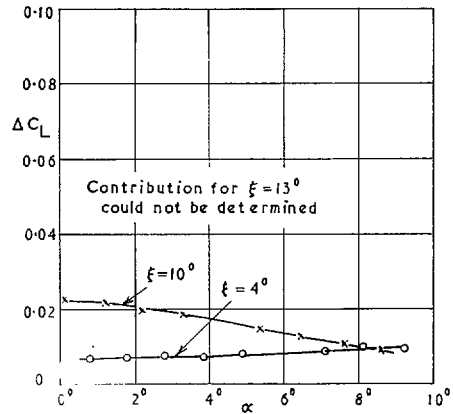
(a) Body contribution   (b) Wing contribution

FIG. 22a and b.   Variation of lift increments with incidence for wing with $\varepsilon = 15°$.
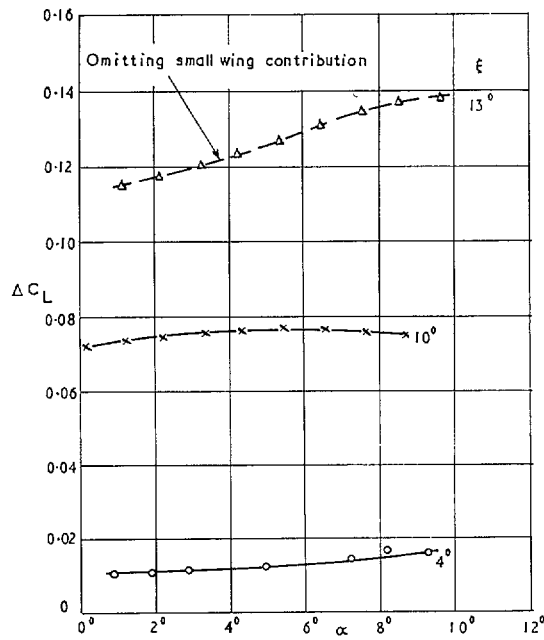
(c)   Total contribution

FIG. 22c.   Variation of lift increments with incidence for wing with $\varepsilon = 15°$ (contd.).

37
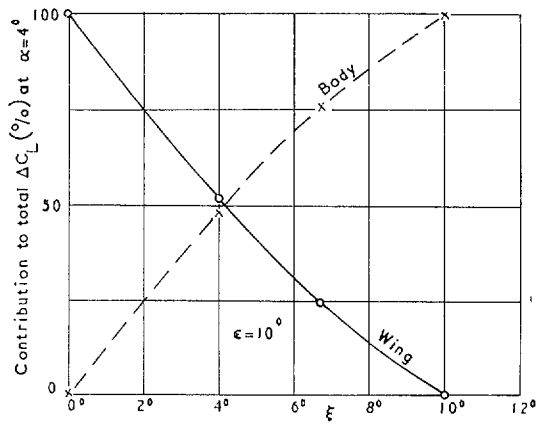
FIG. 23a. Influence, at typical incidence, of cone half-angle on relative contributions
to total lift increment.
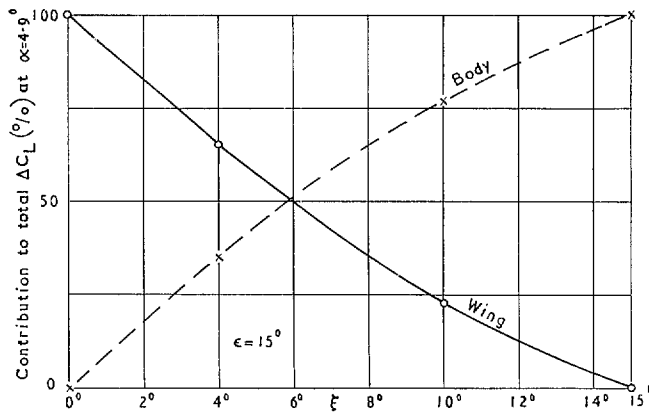
FIG. 23b. Influence, at typical incidence, of cone half-angle on relative contributions
to total lift increment.

38
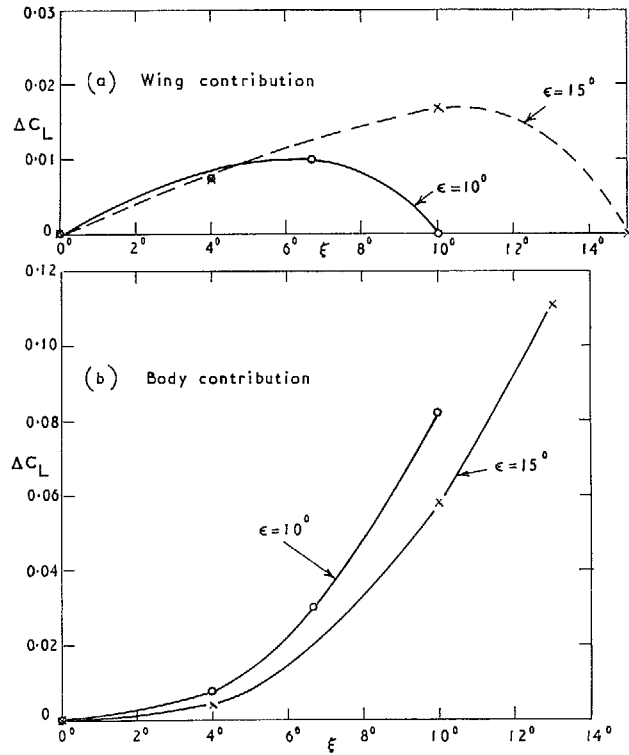
FIG. 24a and b. Influence of wing angle on lift
contributions ($\alpha = 4 \cdot 0°$).
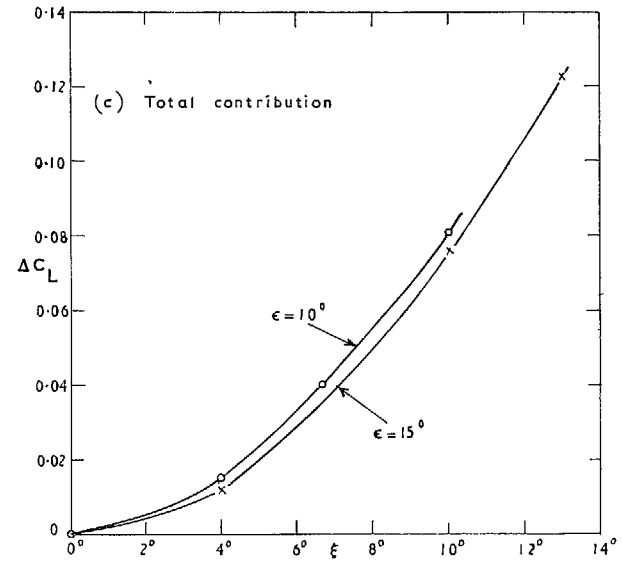
FIG. 24c. Influence of wing angle on lift increment
($\alpha = 4 \cdot 0°$) (contd.).
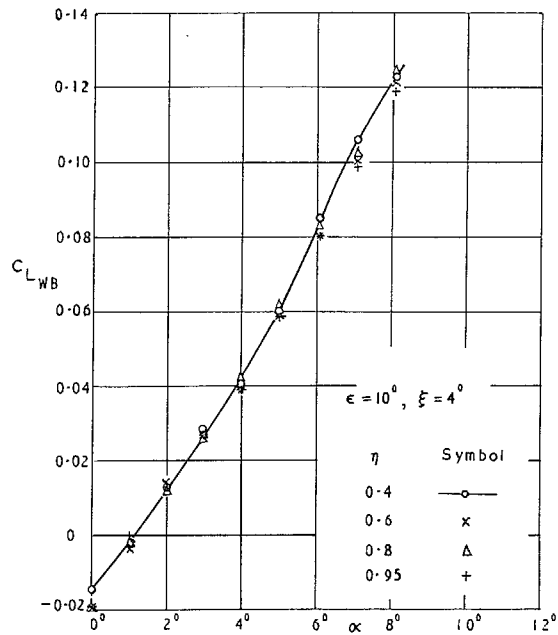
FIG. 25. Effect of chordwise position on total lift of 10°/4° wing-body combination.

(Note: $C_{L_{WB}} = C_{L_W} + \Delta C_L$)
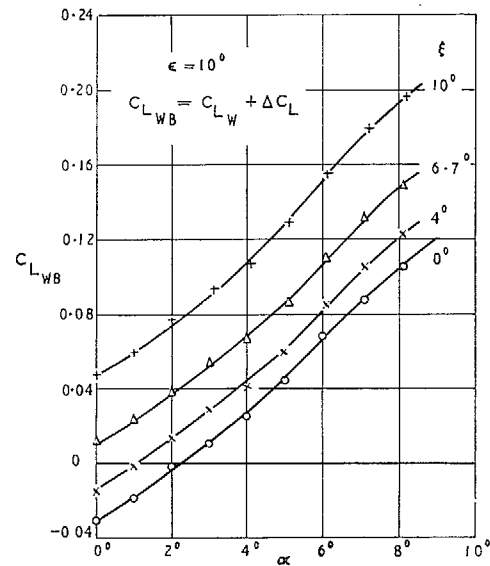
FIG. 26a. Total lift coefficients for four models with $\varepsilon = 10°$ (based on data obtained at $x/c = 0.4$).
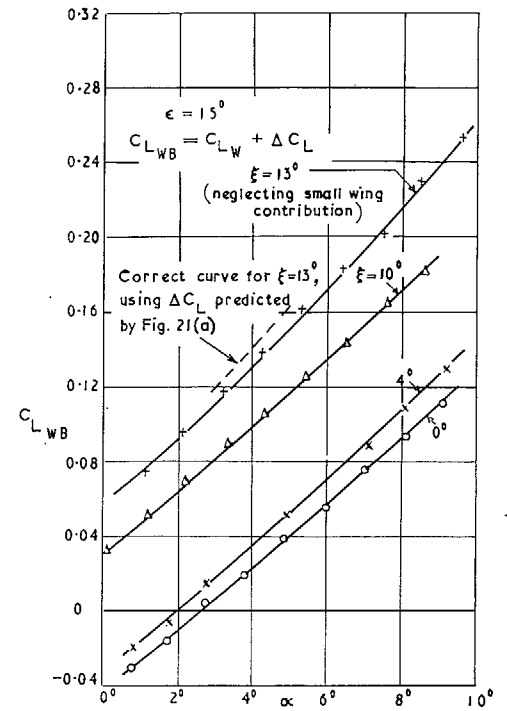
FIG. 26b. Total lift coefficient for four models with $\varepsilon = 15°$ (based on data obtained at $x/c = 0.6$).
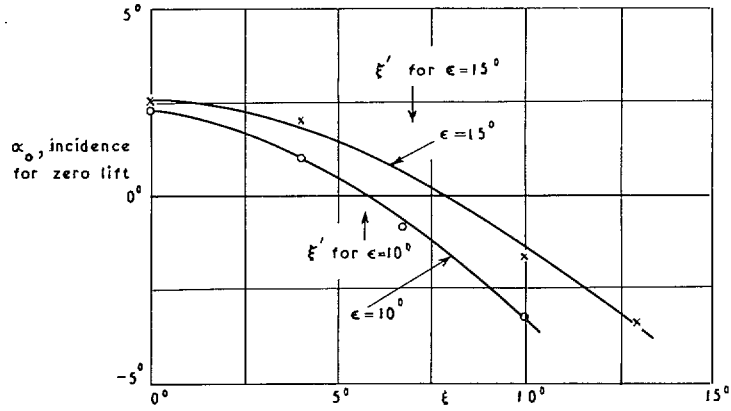
FIG. 27. Influence of cone half-angle on zero-lift incidence; ξ' is the cone half-angle for which the body and wing cross-sectional areas are equal.
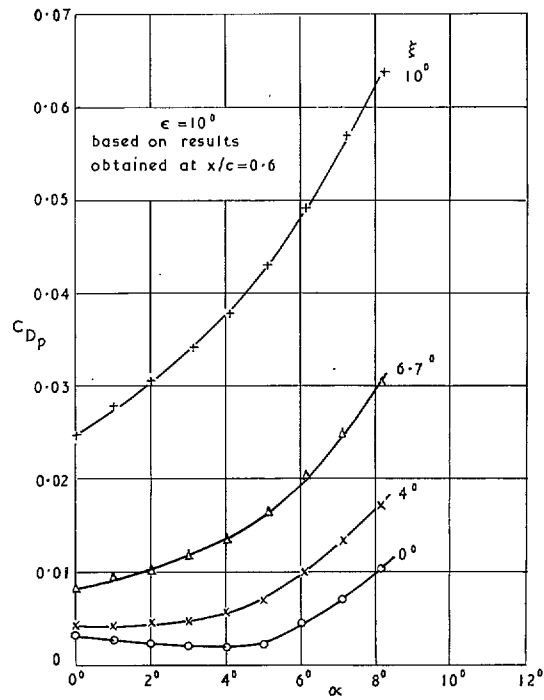
FIG. 28a. Influence of incidence on pressure-drag coefficient (no base drag).

41
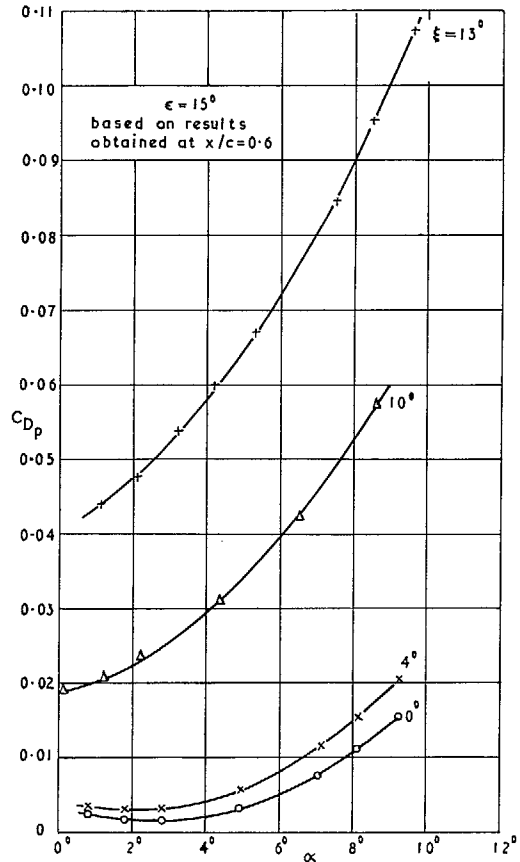
FIG. 28b.   Influence of incidence on pressure-drag coefficient (no base drag).
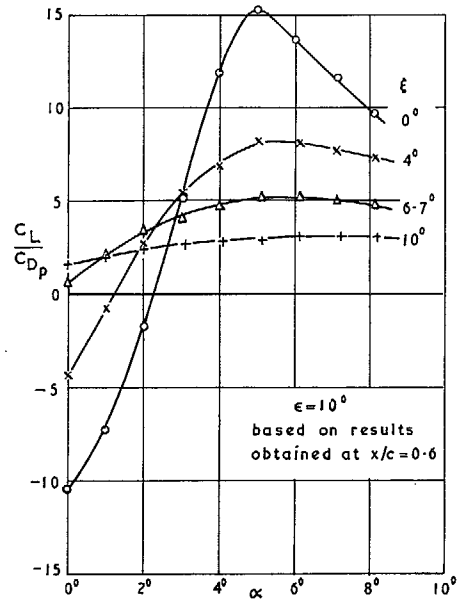
FIG. 29a.   Influence of cone half-angle on lift/pressure-drag ratio.
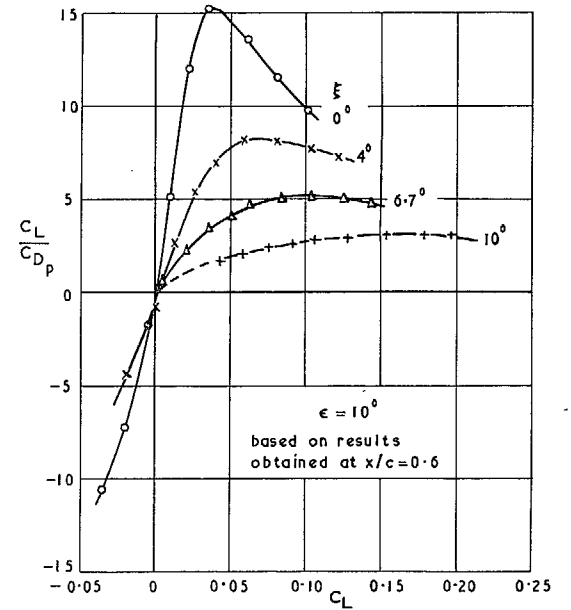
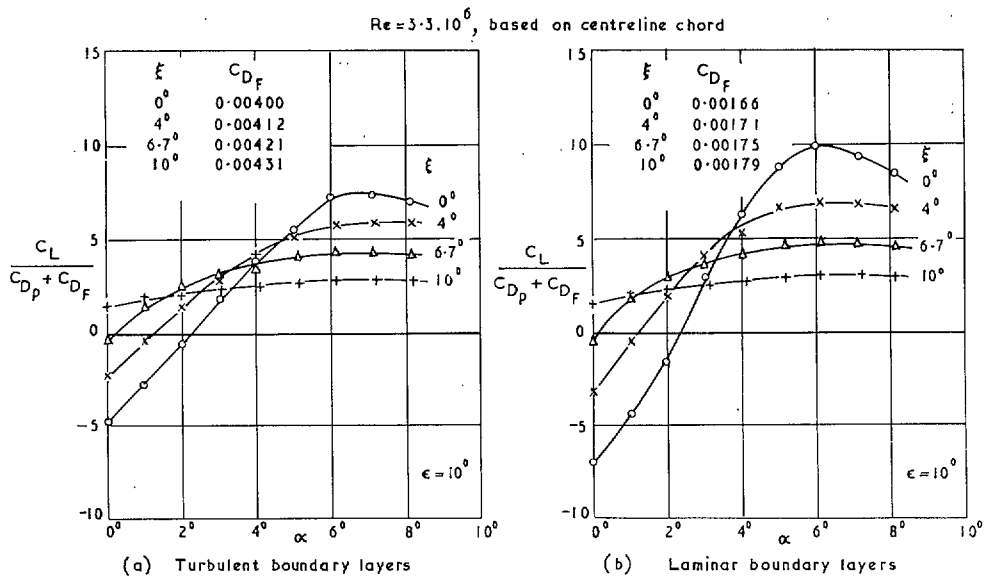FIG. 29b.   Influence of cone half-angle on lift/pressure-drag ratio.
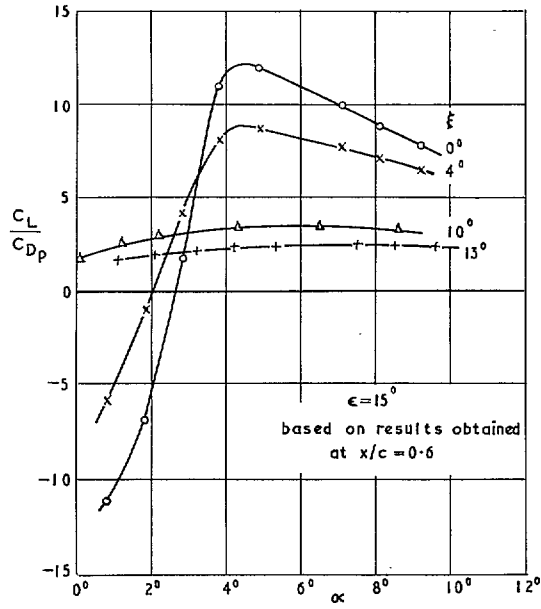
FIG. 30a.   Influence of cone half-angle on lift/pressure-drag ratio.
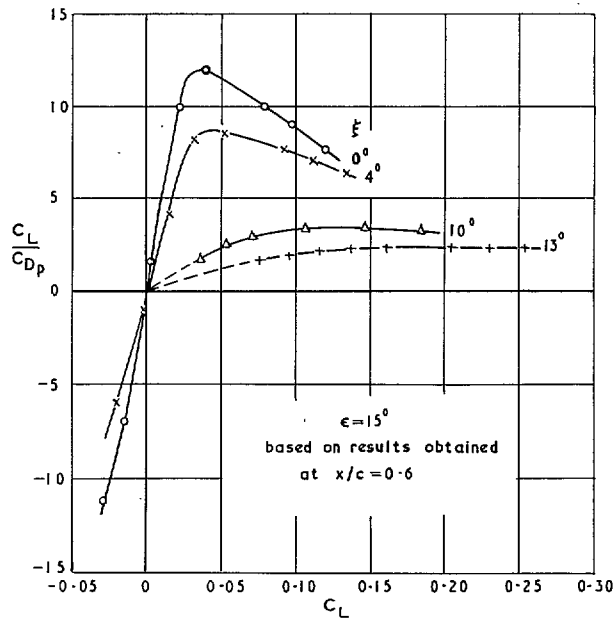
FIG. 30b.   Influence of cone half-angle on lift/pressure-drag ratio.

43

FIG. 31.   Influence of boundary-layer state on lift/drag curves (based on results obtained at $x/c = 0.6$).
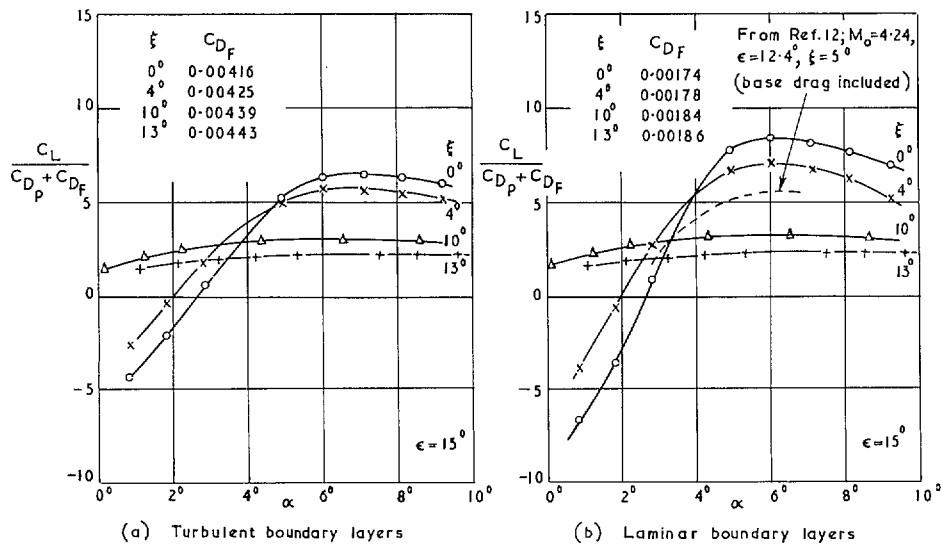
FIG. 32.   Influence of boundary-layer state on lift/drag ratios (based on results obtained at $x/c = 0.6$).

44

(a) Variation of maximum lift/drag ratio with
cone half-angle

(b) Variation of C_L for $(L/D)_{max}$ with
cone half-angle

FIG. 33.   Effect of cone half-angle on maximum lift/drag characteristics.

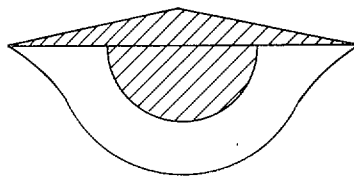(a) Variation of maximum lift/drag ratio with cone
half-angle

(b) Variation of C_L for $(L/D)_{max}$ with cone half-angle
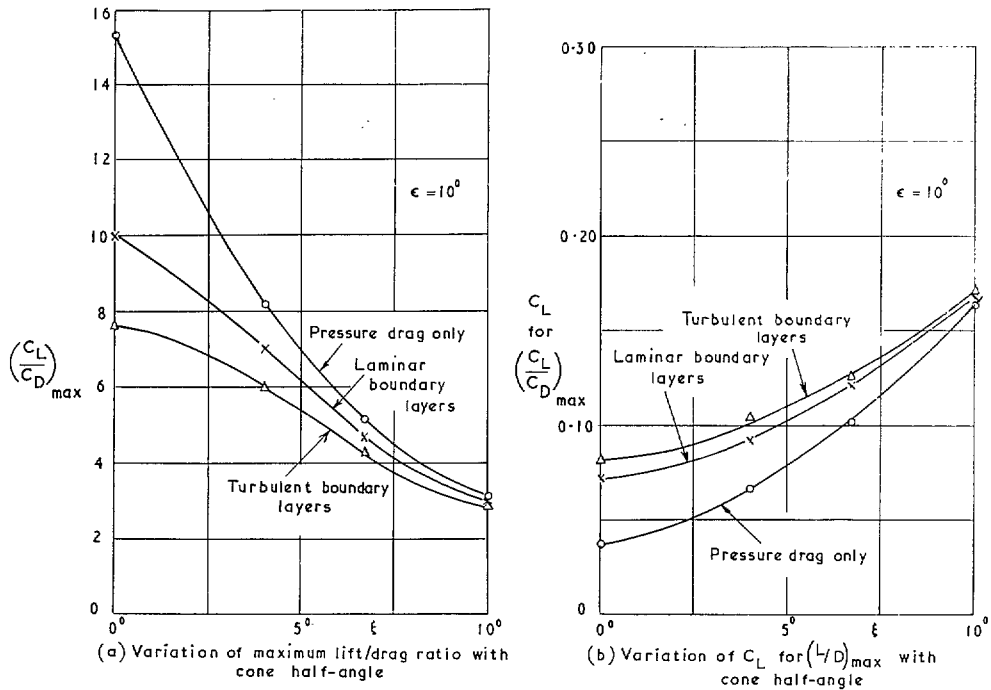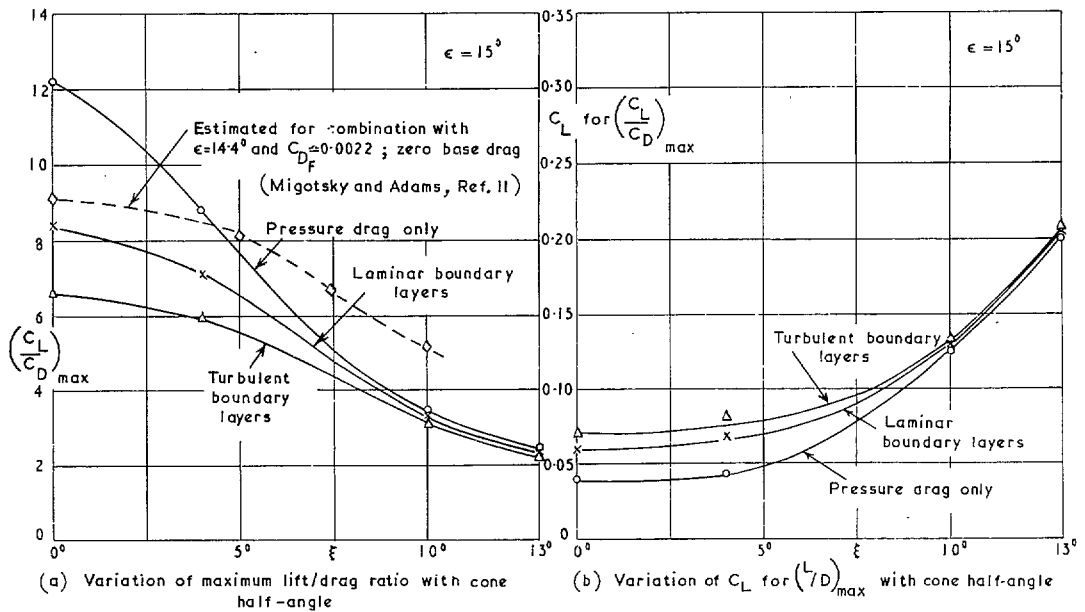
FIG. 34.   Effect of cone half-angle on maximum lift/drag characteristics.
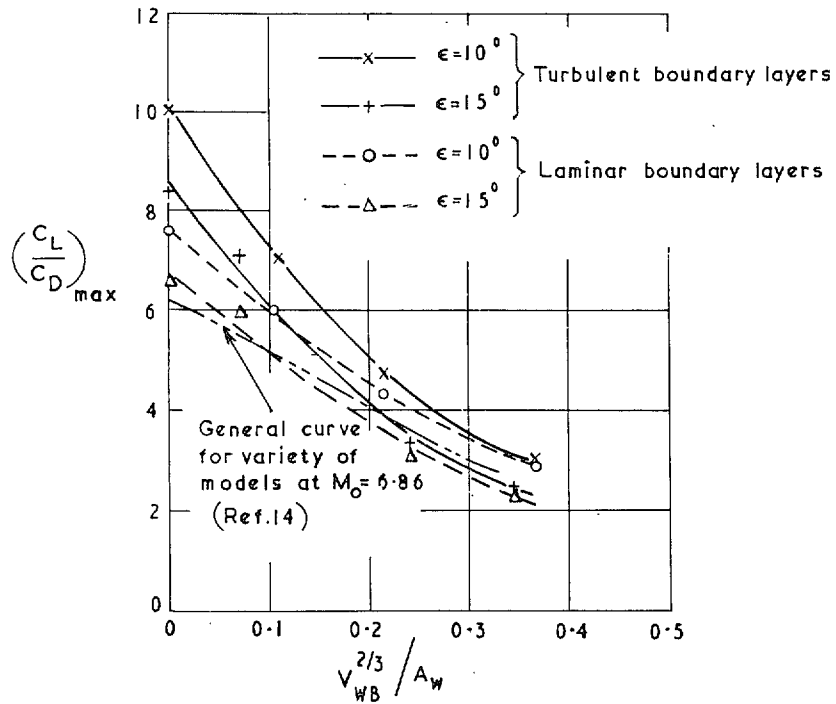
FIG. 35. Suggested correlation parameter for wing-body combinations.
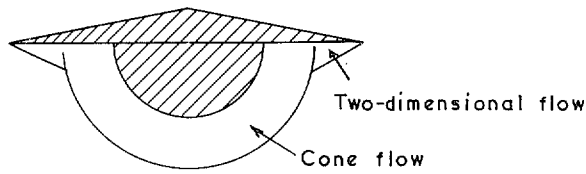
(a) Two-shock pattern

(b) Single-shock pattern

FIG. 36. Lower-surface shock patterns likely on lifting wing-cone vehicles at high supersonic speeds.